CrossMark

ORIGINAL PAPER

Zircon Lu-Hf isotope systematics and U–Pb geochronology, whole-rock Sr-Nd isotopes and geochemistry of the early Jurassic Gokcedere pluton, Sakarya Zone-NE Turkey: a magmatic response to roll-back of the Paleo-Tethyan oceanic lithosphere

Orhan Karsli[1] · Abdurrahman Dokuz[2] · Raif Kandemir[1]

Abstract The early Mesozoic was a critical era for the geodynamic evolution of the Sakarya Zone as transition from accretion to collision events in the region. However, its complex evolutionary history is still debated. To address this issue, we present new in situ zircon U–Pb ages and Lu-Hf isotope data, whole-rock Sr-Nd isotopes, and mineral chemistry and geochemistry data of plutonic rocks to better understand the magmatic processes. The Gokcedere pluton is mainly composed of gabbro and gabbroic diorite. LA-ICP-MS zircon U–Pb dating reveals that the pluton was emplaced in the early Jurassic (177 Ma). These gabbros and gabbroic diorites are characterized by relatively low SiO_2 content of 47.09 to 57.15 wt% and high Mg# values varying from 46 to 75. The samples belong to the calc-alkaline series and exhibit a metaluminous I-type character. Moreover, they are slightly enriched in large ion lithophile elements (Rb, Ba, Th and K) and light rare earth elements and depleted in high field strength elements (Nb and Ti). Gabbroic rocks of the pluton have a depleted Sr-Nd isotopic composition, including low initial $^{87}Sr/^{86}Sr$ ranging from 0.705124 to 0.705599, relatively high ε_{Nd} (t) values varying from 0.1 to 3.5 and single-stage Nd model ages (T_{DM1} = 0.65–0.95 Ga). In situ zircon analyses show that the rocks have variable and positive ε_{Hf} (t) values (4.6 to 13.5) and single-stage Hf model ages (T_{DM1} = 0.30 to 0.65 Ga). Both the geochemical signature and Sr-Nd-Hf isotopic composition of the gabbroic rocks reveal that the magma of the studied rocks was formed by the partial melting of a depleted mantle wedge metasomatized by slab-derived fluids. The influence of slab fluids is mirrored by their trace-element characteristics. Trace-element modeling suggests that the primary magma was generated by a low and variable degree of partial melting (~5–15%) of a depleted and young lithospheric mantle wedge consisting of phlogopite- and spinel-bearing lherzolite. Heat to melt the mantle material was supplied by the ascendance of a hot asthenosphere triggered by the roll-back of the Paleo-Tethyan oceanic lithosphere. The rising melts were accompanied by fractional crystallization and encountered no or minor crustal contamination en route to the surface. Taking into account these geochemical data and integrating them with regional geological evidence, we propose a slab roll-back model; this model suggests that the Gokcedere gabbroic pluton originated in a back-arc extensional environment associated with the southward subduction of the Paleo-Tethyan oceanic lithosphere during the early Jurassic period. Such an extensional event led to the opening of the northern branch of the Neotethys as a back-arc basin. Consequently, we conclude that the gabbroic pluton was related to intensive extensional tectonic events, which peaked during the early Jurassic in response to the roll-back of Paleo-Tethyan oceanic slab in the final stage of oceanic closure.

Keywords Gabbroic pluton · Depleted mantle · Early Jurassic pluton · Sakarya Zone-NE Turkey

✉ Orhan Karsli
okarsli@gmail.com

1 Department of Geological Engineering, Recep Tayyip Erdogan University, 53000 Rize, Turkey

2 Department of Geological Engineering, Gumushane University, 29000 Gumushane, Turkey

Introduction

The Sakarya Zone, which is one of the main tectonic branch of Anatolia, preserves unique tectono-magmatic records to understand Cimmerian tectonic events in the region. However, the Cimmerian Orogeny is still open to debate regarding the rarity of intrusive rocks and the absence of systematic geochronological data. Moreover, the separation of the Cimmerian continental fragment from Gondwana is attributed to the late Permian to early Triassic period (Robertson et al. 2004; Topuz et al. 2013). A major dilemma here is the subduction polarity throughout the closure of the Paleo-Tethyan Ocean. Northward (Robertson et al. 2004; Mackintosh and Robertson 2009; Topuz et al. 2013) and southward (Sengor and Yilmaz 1981; Sengor et al. 1984; Goncuoglu et al. 2004) models have been proposed regarding the polarity of the subduction. In this context, it is believed that subduction of the Paleo-Tethyan oceanic lithosphere commenced in the late Carboniferous to early Permian period (Karsli et al. 2016) and continued during the early Mesozoic era. However, the cessation time of its subduction remains controversial. Intrusive rocks are considered a considerable component of the continental crust, which records crustal evolution and crust-mantle processes in response to different geodynamic conditions. Thus, the early Mesozoic, which was a crucial period of Paleo-Tethyan oceanic crust subduction, may have recorded the final stage that led the termination of subduction of the Paleo-Tethyan oceanic lithosphere. Although Mesozoic-Cenozoic granitoids are well documented (e.g., Yilmaz and Boztug 1996; Topuz et al. 2005; Karsli et al. 2007, 2010a, 2011, 2012a, b; Kaygusuz et al. 2008; Aydin 2014), the granitoids formed in the late Triassic to Jurassic era are relatively poorly understood. More recently, igneous rocks in the region from the early to middle Jurassic have been intensively researched (Dokuz et al. 2006; Karsli et al. 2014). The researchers consensually believe that late Triassic to early Jurassic magmatism was formed by the partial melting of the mantle wedge in a subduction setting in the region. More recently, Dokuz et al. (2010, 2017a) reported middle to late Jurassic magmatic activities as a response to slab-break of the Paleo-Tethyan oceanic lithosphere during the Cimmerian Orogeny. However, the final closure time of the Paleo-Tethyan Ocean has long been unclear due to sporadic magmatic activity in the late Triassic to early Jurassic period. Indeed, the systematic petrochemical signature of early Jurassic intrusive rocks is a useful tool to resolve the dilemma of subduction polarity and the final stage of Paleo-Tethyan oceanic subduction, which points to a transition from accretion to a collision event in a dynamic system. Thus, much more precise data are needed to verify this tectonomagmatic framework of Cimmerian events.

In this contribution, we investigated a body of early Jurassic gabbroic to gabbroic diorite rocks preserving essential clues to its tectonic evolution. This enables us to study subduction events of the Paleo-Tethyan oceanic lithosphere during the early Mesozoic in the eastern Sakarya Zone, Turkey. We present the new LA-ICP-MS zircon U–Pb ages and in situ Lu-Hf isotopes, mineral composition, geochemical data, and whole-rock Sr-Nd isotope systematics of the gabbroic pluton with the objectives of: (1) constraining their emplacement age; (2) deciphering the nature of the magma source and magma evolution; and (3) determining the tectonic setting and implications for Paleo-Tethyan magmatic activity during the early Jurassic period. The obtained data will enable us to better understand the geodynamic setting and tectonic significance in the context of the final stage of subduction of the Paleo-Tethyan Ocean during the Cimmerian Orogeny.

Geological background of the eastern Sakarya Zone

The Sakarya Zone, one of the main tectonic units of Anatolia, was separated by ophiolitic suture zones (e.g., Okay and Tuysuz 1999). It is characterized by east–west trending Alpine continental fragments that run approximately 1400 km from Lesser Caucausus to the Aegean coast, along northern Anatolia (Fig. 1a). This zone is surrounded to the northwest by the Rhodope-Strandja, Istanbul, and Zonguldak Zones, and the Central and Eastern Pontides. The Sakarya Zone is bound by the Anatolid-Tauride block along ophiolites of the Izmir-Ankara-Erzincan Suture zone to the south. The eastern part of the Sakarya Zone, known as the Eastern Pontides, is a well-preserved large mountain belt measuring 500 km long and 100 km wide. The northeast boundary is marked by the Achara-Trialet belt. The Great Caucasus lies to the north and the Taurides to the south. The basement of the eastern Sakarya Zone is composed of early Carboniferous to early Permian intrusives (e.g., Okay and Leven 1996; Topuz et al. 2007, 2010; Dokuz 2011; Kaygusuz et al. 2012; Karsli et al. 2016; Dokuz et al. 2017b) and metamorphic rocks (Topuz et al. 2004, 2007; Okay et al. 2006). This basement is unconformably overlain by Permo-Carboniferous clastic sedimentary rocks (Capkinoglu 2003; Kandemir and Lerosey-Aubril 2011). Recently, a few upper-mantle serpentinized lherzolite and harzburgite blocks (up to 300 m^2) belonging to the Variscan basement of the eastern Sakarya Zone were observed in the Beycam (Gumushane area) and Pulur (Bayburt area) areas (Dokuz et al. 2011). The

Fig. 1 a Main tectonic branches of Anatolia in relation to the Afro-Arabian and Eurasian plates [after Okay and Tuysuz (1999)]. **b** Detailed geological map of the Gokcedere area exhibiting stratigraphic relationships of the calc-alkaline gabbroic Gokcedere pluton
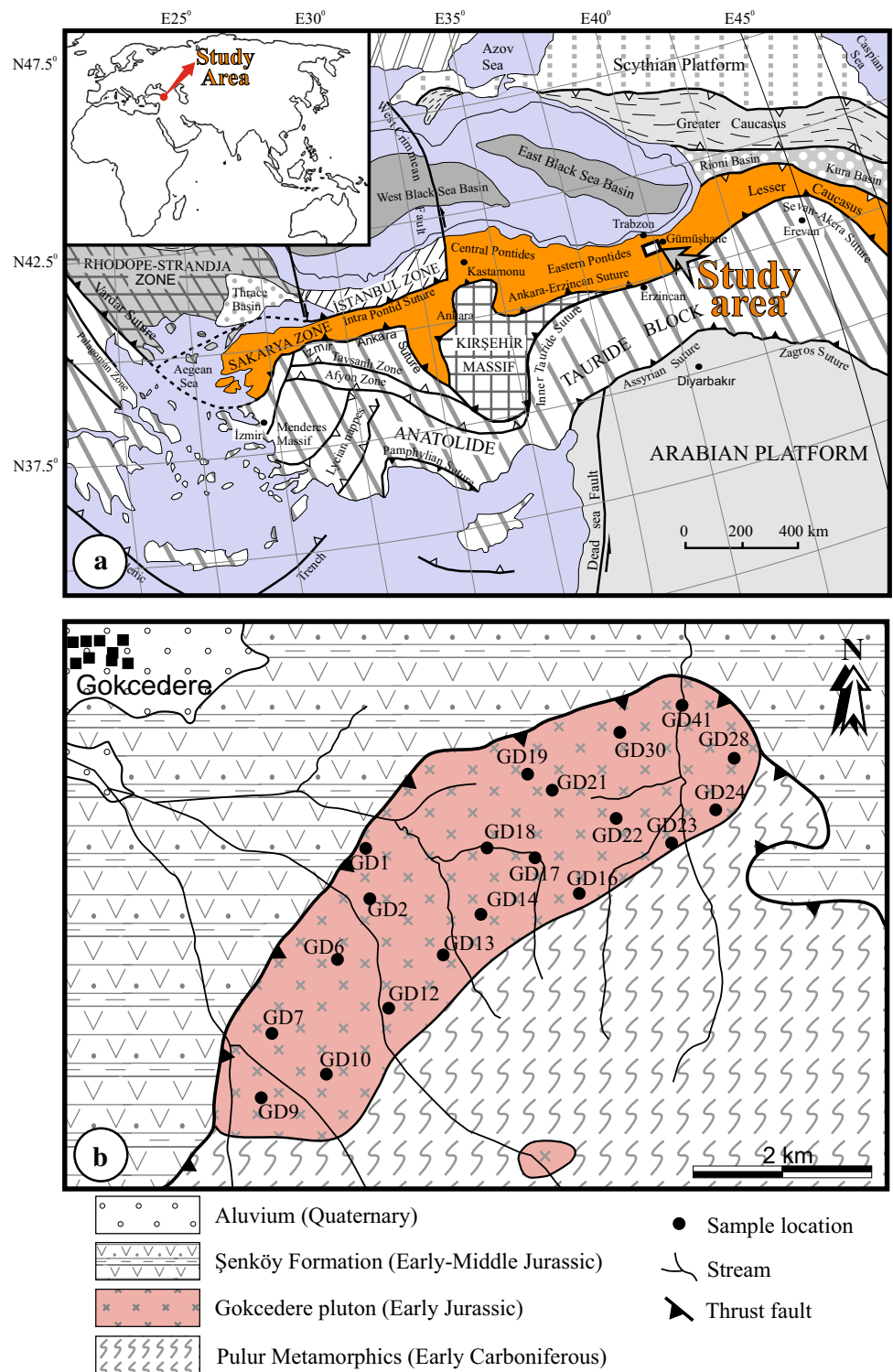
Variscan metamorphic-magmatic basement is unconformably overlain by post Triassic volcano-sedimentary rocks (Dokuz and Tanyolu 2006; Sen 2007; Kandemir and Yilmaz 2009). Late Triassic events in the western part of the Sakarya Zone have been interpreted as associated with a subduction setting, based on the blueschists and eclogites of the Karakaya complex (Okay et al. 2002; Okay and Goncuoglu 2004). This period is poorly understood due to the rarity of late Triassic intrusive rocks in the eastern part of the Sakarya Zone (Eyuboglu et al. 2011; Karsli et al. 2014). Based on the geochemical signature of the intrusive (Dokuz et al. 2006; Ustaomer and

Robertson 2010) and volcanic (Sen 2007) rocks, it is suggested that the late Triassic to the early Jurassic period was dominated by a continental magmatic arc separated from the northern margin of Gondwana during the early Triassic in response to the southward subduction of the Paleotethyan oceanic slab (Sengor and Yilmaz 1981; Yilmaz et al. 1997; Kocyigit and Altiner 2002; Dokuz et al. 2006, 2010). This southward subduction of the Paleo-Tethyan oceanic slab caused the formation of the northern branch of the Neotethys Ocean in the southern part of the Sakarya Zone (Sengor and Yilmaz 1981). Middle to late Jurassic granitoids and dacites emplaced within the volcano-sedimentary rocks of the Şenköy Formation (Dokuz et al. 2006, 2010) together with molasse sediments are believed to be the products of an arc-continent collision in response to the closure of the Paleotethys during the middle Jurassic period and the accretion of the Sakarya Zone onto Laurasia in the north (Sengor et al. 1980; Sengor and Yilmaz 1981; Yilmaz et al. 1997; Dokuz et al. 2010, 2017a). The late Jurassic to early Cretaceous period was characterized by platform carbonates of the Berdiga Formation (Gorur 1997; Tuysuz 1999). During the late Cretaceous period, the opening of the Black Sea in the northern part of the Sakarya Zone was triggered by the northward subduction of the Neo-Tethyan oceanic lithosphere beneath the Sakarya Zone (Okay et al. 1994; Robinson et al. 1995; Sengor et al. 2003; Kaygusuz et al. 2008; Karsli et al. 2010a, 2012a; Aydin 2014). This subduction resulted in a submarine magmatic arc (Okay and Sahinturk 1997; Yilmaz et al. 1997; Okay and Tuysuz 1999; Boztug et al. 2004; Altherr et al. 2008; Boztug and Harlavan 2008; Kaygusuz et al. 2008; Cinku et al. 2010; Ustaomer and Robertson 2010; Karsli et al. 2010a, 2012a). The flyschoid sedimentary rocks combined with limestone deposited in the southern part of the region are indicative of being a fore-arc system in the south. The early Paleocene plagioleucitites in the region have been interpreted as the final products of the northward subduction (Altherr et al. 2008). The Paleocene and early Eocene period in the eastern Sakarya Zone were dominated by a continent–continent collision between the Sakarya and the Tauride-Anatolide blocks in response to the complete closure of the Neo-Tethyan Ocean (Okay and Sahinturk 1997; Boztug et al. 2004; Hisarli 2011; Karsli et al. 2010b, 2011; Topuz et al. 2005; Rolland et al. 2012). Middle Eocene high-K calc-alkaline intrusives have been credited with the orogenic collapse, following slab-break-related rapid uplift (Boztug et al. 2004, 2006; Karsli et al. 2007, 2012b; Aydincakir and Sen 2013). Additionally, Neogene volcanism was thought to have formed in a continental extensional setting in the region (Aydin et al. 2008, 2009; Dokuz et al. 2013).

Analytical procedure

Mineral composition

To decipher mineralogical features and measure micro chemical compositions, polished thin sections were prepared at the Ludwig Maximillian University, Department of Mineralogy, Petrology and Geochemistry, Munich (Germany). The micro chemical analyses were performed using a Cameca SX-100 electron microprobe equipped with five wavelength-dispersive spectrometers at Department of Mineralogy, Petrology and Geochemistry, Munich (Germany). The analytical conditions included accelerating voltage of 15 kV, a beam current of 20 nA, and a counting time of 10 to 30 s. Synthetic and natural oxides and silicates were used as standard materials. The correction procedures were based on the CAMECA PAP algorithm by Pouchou and Pichoir (1985). The detection limits were generally on the order of 0.1 wt%. The counting time was usually set to 10 s when analyzing for the major elements (Si, Al, Fe, Mg, Mn, Ca, Na, K, Cr, and Ti). The analyses were performed using a beam diameter of 1 μm, except in the case of feldspars, when a defocused beam (10 μm) was used to minimize the alkaline diffusion.

LA-ICP-MS zircon U–Pb analysis

Two zircon-bearing gabbroic samples were crushed. The zircons were separated by the hydro separation and electromagnetic separation techniques and then the zircon grains were selected under a binocular microscope at the Key Laboratory of Orogenic Belts and Crustal Evolution, Peking University, Beijing. Cathodoluminescence (CL) images were prepared to check the internal structures of individual zircon grains and spots were selected for analysis at the same laboratory. Zircon U–Pb analyses were carried out on a Finnigan Neptune MC-ICP-MS and New Wave UP213 LA-MC-ICP-MS housed at the Institute of Mineral Resources in the Chinese Academy of Geological Sciences, Beijing, China. Zircon GJ-1 was used as an external standard. The analytical procedure and details are outlined in Hou et al. (2009). Spot diameters were 25 μm. The U, Th, and Pb abundances were measured in reference to the values in standard zircon M127 ($U = 923 \times 10^{-6}$; $Th = 439 \times 10^{-6}$; $Th/U = 0.475$) (Nasdala et al. 2008). The ICP-MS Data Cal Software described by Liu et al. (2008) was used for raw data calculations of the measurements.

Whole-rock major and trace-element analysis

Twenty fresh gabbro and gabbroic diorite samples were collected at the pluton near Gokcedere village (Demirozu-Bayburt) in northeast Turkey (Fig. 1b) for whole-rock

major and trace-element analyses. All the samples were megascopically fresh, undeformed, and unmetamorphosed. To prepare the rock powders, 1–3 kg of each sample was initially crushed in a steel crusher and then the samples were manually fine-powdered in an agate mortar to reduce the grain size to <200 mesh. Analyses of the major oxide and trace elements of the samples were performed at the commercial facilities of ACME Laboratories Ltd., Vancouver (Canada). The amounts of major element oxides were measured using a Perkin-Elmer Elan 600 ICP-AES (0.2 g of pulp sample by $LiBO_2$ fusion). The detection limits are approximately 0.001–0.04%. To measure trace-element abundances, 0.2 g of sample powder and 1.5 g of $LiBO_2$ flux were mixed in a graphite crucible and heated to 1050 °C for 15 min in a muffle furnace. The molten sample was then dissolved in 100 mL of 5% HNO_3 (American Chemical Society-grade nitric acid in deionized water). The sample solutions were shaken for 2 h and then an aliquot was poured into a polypropylene test tube and aspirated into a Perkin-Elmer Elan 600 ICP mass spectrometer. Calibration and verification standards, together with reagent blanks, were added to the sample sequence. The elemental concentrations of the samples were obtained using BCR-2 and BIR-2 (concentrations from USGS) as external standards. The detection limits ranged from 0.01 to 0.5 ppm for most of the trace elements.

In situ zircon Lu-Hf isotope analysis

In situ zircon Lu-Hf isotopic analyses were conducted at Institute of Mineral Resources in the Chinese Academy of Geological Sciences, Beijing, China. They were carried out on a Neptune MC-ICP-MS in combination with a New Wave UP213 laser ablation inductively coupled plasma spectrometer (LA-MC-ICP-MS). The analyses were carried out on the same spots or domains adjacent to where U–Pb dating was done. The size of laser-ablated spots was 50 μm when the laser repetition rate was 10 Hz. Throughout the analyses, isobaric interference of ^{176}Lu on ^{176}Hf was corrected based on measured ^{175}Lu values. ^{176}Yb/^{172}Yb values of 0.5887 and the mean β_{Yb} value were used to correct for the interference of ^{176}Yb on ^{176}Hf (Wu et al. 2006).

Whole-rock Sr-Nd isotope analysis

The powdered samples of bulk rocks were dissolved using acid (HF + $HClO_4$) in sealed Savillex beakers on a hot plate for 1 week. Separation of Rb, Sr, and light rare earth elements (REEs) was done through a cation-exchange column (packed with Bio-Rad AG5OWx8 resin). Sr and Nd isotopic analyses were performed at the Institute of Geology and Geophysics, Chinese Academy of Sciences, Beijing. Isotope analyses were carried out using a multi-collector

VG354 mass spectrometer. Rb, Sr, Sm, and Nd concentrations were measured using the isotopic dilution method. ^{87}Sr/^{86}Sr ratios were normalized against ^{86}Sr/^{88}Sr = 0.1194, and ^{143}Nd/^{144}Nd ratios were normalized against ^{146}Nd/^{144}Nd = 0.7219. ^{87}Sr/^{86}Sr ratios were adjusted to the NBS-987 Sr standard = 0.710250, and ^{143}Nd/^{144}Nd ratios were adjusted to the La Jolla Nd standard = 0.511860. The precision in concentration analyses by isotopic dilution was ±2% for Rb, ±0.4 to 1% for Sr, and <±0.5% for Sm and Nd, depending on concentration levels; overall precision for Rb/Sr was ±2% and for Sm/Nd was ±0.2 to 0.5%. Procedural blanks were Rb = 120 pg, Sr = 200 pg, Sm = 50 pg, and Nd = 50–100 pg. The detailed analytical procedures for Sr and Nd isotopic measurements are outlined in Qiao (1988).

Results

Brief petrography, mineralogy, and mineral composition.

Twenty gabbroic samples were collected from the Gokcedere pluton with an exposure area of ~20 km², which was emplaced in the early Carboniferous Pulur metamorphics near Gokcedere village, Demirozu-Bayburt area, northeast Turkey. The sample locations and their latitude and longitude are depicted in Fig. 1b. All the samples were megascopically fresh, undeformed, and unmetamorphosed. The individual pluton showed sharp contacts with early Carboniferous metamorphic basement rocks and is overlined by the volcano-sedimentary rocks of the Şenköy Formation (Fig. 1b). The gabbroic body was predominantly medium-grained gabbro, with a more evolved gabbroic diorite (Fig. 2a). These lithologies showed gradational relationships manifested by spatial variation in mineral modal abundances. The intrusive samples were fresh and undeformed. No mafic micro granular enclaves were observed within the host rocks, and the samples exhibited no evidence of magma mixing, such as ocellar quartz, spongy plagioclase, or disequilibrium textures around the other minerals. The samples from the pluton were dark to dark gray, with a medium-grained texture composed of euhedral to anhedral plagioclase, quartz, K-feldspar and amphibole, usually accompanied by ilmenite and zircon (Fig. 2b). Clear cumulus textures were lacking in the samples. Plagioclase was observed to occur as large euhedral to subhedral crystals with no exhibited chemical zoning (~2 mm; Fig. 2c, d). They showed heterogeneous composition ranging from An_8 to An_{74}, with Or content rarely exceeding 2 mol% (Supplementary Table 1). K-feldspar ($Or_{86-93}Ab_{1-14}An_{0-1}$), which never exceeded 4% in the modal composition, formed as subhedral to anhedral crystals and contained
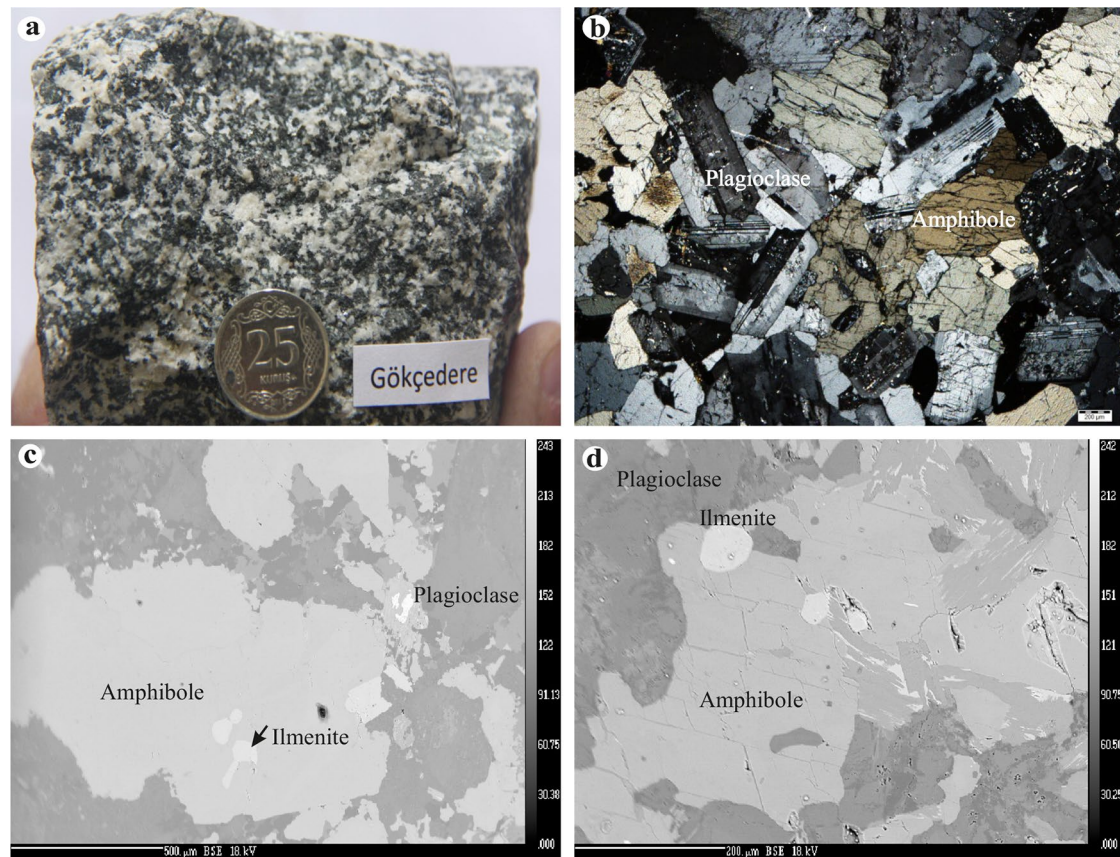
Fig. 2 a Macroscopic view showing petrographical features of the pluton (Sample GD19; gabbro). **b** Microphotograph (under cross polarization) view exhibiting textural relationships of the gabbroic rocks. **c, d** BSE views displaying textural relationships of the gabbroic rocks. Minerals include amphibole, plagioclase, quartz and ilmenite. The diameter of 25 coin is 2 cm

small plagioclase, quartz, and amphibole crystals, which represent poikilitic textures (Fig. 2c, d). The quartz was anhedral with irregular cracks and interstitial to the other minerals (Fig. 2c, d). Green to brownish-green amphiboles were generally anhedral, with inclusions of Fe-Ti oxide (Fig. 2c, d). They were generally calcic and characterized by X_{Mg} [$=Mg/(Mg+Fe_{tot})$]$=0.49-0.74$ (Supplementary Table 1). Ilmenites and magnetite were present as poikilitic inclusions within mafic silicates, and were of homogeneous composition ($Ilm_{97}Hm_{03}$; $Mt_{95-75}Usp_{25-05}$) (Fig. 2b–f; Supplementary Table 1). Zircon was an accessory phase in all rock types and occurred as prismatic crystals (Fig. 3).

Zircon U–Pb ages

Zircon grains selected from the samples GD1 (gabbro) and GD23 (gabbroic diorite) were euhedral to subhedral and colorless and had mostly prismatic morphologies. The grains exhibited pyramidal termination and oscillatory zoning patterns with a length of ~50–350 μm, which suggests a magmatic origin. Some zircons exhibited a dark-gray color and had heterogeneous fractured domains (Fig. 3).

Based on the CL images, zircons free of visible inclusions were chosen for U–Pb dating analyses; the data is provided in Table 1 and shown on a concordia diagram (Fig. 3). A total of 30 spots from the 28 zircons were measured from the sample. As shown in Table 1 and Fig. 3, concordant analyses yielded weighted mean ages of 176.95 ± 0.49 Ma (MSWD $= 1.08$) from the gabbro samples (GD1) and 178.41 ± 0.44 Ma (MSWD $= 1.10$) from the gabbroic diorite sample (GD23) of the Gokcedere pluton, revealing its emplacement age.

Geochemistry

Major elements

A complete data set of whole-rock major element analyses for the representative samples from the studied gabbroic rocks is given in Table 2. Most of the samples have low loss on ignition values in a moderate range of 0.90–2.80 wt%, which suggests minimal weathering secondary processes and no hydrothermal alteration. Therefore, they can be used to document the petrogenesis of the Gokcedere pluton. The
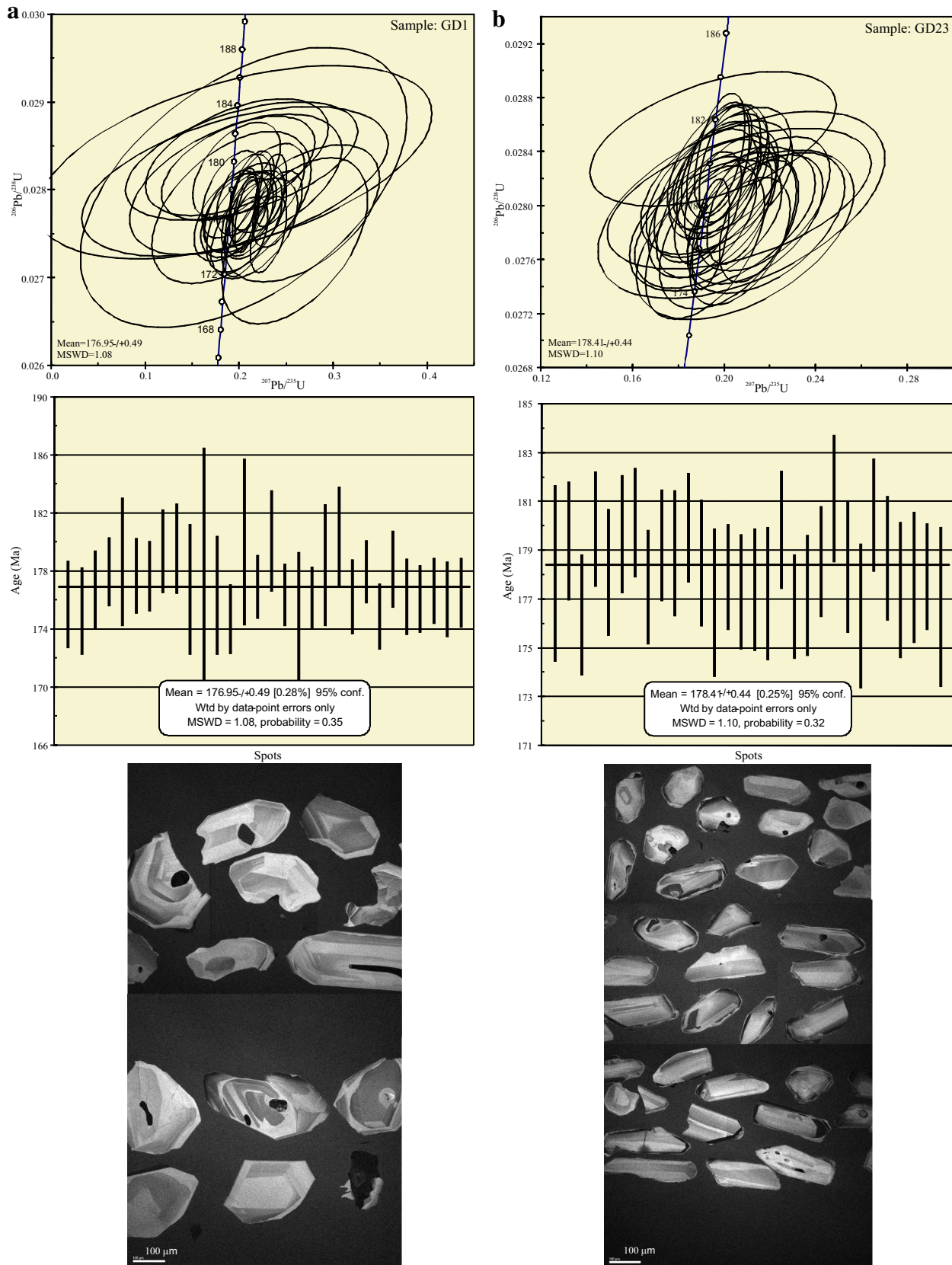
Fig. 3 In situ zircon LA-ICP-MS U–Pb age concordia and average age diagram of the Gokcedere pluton. *Inset* representative CL images of zircons from samples GD1 (gabbro) and GD23 (gabbroic diorite). The *scale bar* is 100 μm

Table 1 LA-ICP-MS U–Pb age data for the zircons of the calc-alkaline Gokcedere gabbroic pluton from the Bayburt area in the eastern Sakarya Zone

Spot	Pb (ppm)	U (ppm)	$^{206}Pb/^{238}U$	1σ	err%	$^{207}Pb/^{235}U$	1σ	err%	$^{207}Pb/^{206}Pb$	1σ	err%
Sample GD23											
1	8	282	0.0280	0.0003	1.01	0.2075	0.0256	12.33	0.0537	0.0068	12.59
2	9	306	0.0282	0.0002	0.68	0.1994	0.0083	4.14	0.0512	0.0021	4.16
3	9	305	0.0277	0.0002	0.70	0.2068	0.0090	4.33	0.0541	0.0023	4.33
4	5	157	0.0283	0.0002	0.65	0.1986	0.0071	3.58	0.0509	0.0019	3.74
5	7	234	0.0280	0.0002	0.73	0.2171	0.0118	5.45	0.0562	0.0031	5.45
6	7	227	0.0283	0.0002	0.67	0.2034	0.0104	5.13	0.0522	0.0026	4.90
7	12	391	0.0283	0.0002	0.62	0.1978	0.0058	2.93	0.0506	0.0015	2.90
8	10	327	0.0279	0.0002	0.66	0.1922	0.0089	4.63	0.0499	0.0023	4.56
9	16	524	0.0282	0.0002	0.63	0.1960	0.0082	4.17	0.0504	0.0021	4.18
10	4	145	0.0281	0.0002	0.72	0.1968	0.0136	6.89	0.0507	0.0034	6.71
11	3	105	0.0283	0.0002	0.62	0.2000	0.0045	2.26	0.0513	0.0012	2.32
12	3	96	0.0281	0.0002	0.72	0.1921	0.0093	4.83	0.0496	0.0024	4.76
13	5	153	0.0278	0.0002	0.85	0.2021	0.0124	6.12	0.0527	0.0032	6.08
14	6	191	0.0280	0.0002	0.61	0.2066	0.0058	2.81	0.0535	0.0015	2.82
15	4	128	0.0279	0.0002	0.66	0.2147	0.0069	3.20	0.0558	0.0017	3.12
16	5	151	0.0279	0.0002	0.70	0.2135	0.0121	5.67	0.0555	0.0031	5.56
17	7	234	0.0279	0.0002	0.77	0.2182	0.0140	6.40	0.0568	0.0037	6.44
18	5	181	0.0283	0.0002	0.67	0.1971	0.0089	4.52	0.0505	0.0022	4.45
19	6	208	0.0278	0.0002	0.60	0.1941	0.0033	1.72	0.0507	0.0009	1.75
20	16	525	0.0279	0.0002	0.69	0.1931	0.0131	6.80	0.0503	0.0035	7.00
21	4	130	0.0281	0.0002	0.63	0.2028	0.0083	4.07	0.0524	0.0021	4.06
22	2	77	0.0285	0.0002	0.71	0.1952	0.0220	11.25	0.0497	0.0058	11.64
23	6	202	0.0281	0.0002	0.76	0.2065	0.0235	11.39	0.0534	0.0061	11.44
24	3	109	0.0277	0.0002	0.84	0.1915	0.0106	5.54	0.0501	0.0027	5.46
25	10	338	0.0284	0.0002	0.64	0.1980	0.0045	2.27	0.0506	0.0011	2.25
26	23	771	0.0281	0.0002	0.71	0.1949	0.0118	6.04	0.0503	0.0030	6.02
27	30	1014	0.0279	0.0002	0.78	0.1992	0.0166	8.33	0.0518	0.0043	8.37
28	5	159	0.0280	0.0002	0.75	0.1947	0.0114	5.85	0.0505	0.0029	5.80
29	7	225	0.0280	0.0002	0.61	0.1930	0.0060	3.10	0.0500	0.0015	3.08
30	7	229	0.0278	0.0003	0.92	0.2091	0.0194	9.27	0.0546	0.0038	6.94

Spot	$^{208}Pb/^{232}Th$	1σ	err%	$^{232}Th/^{238}U$	1σ	err%	$^{206}Pb/^{238}U$ (age)	1σ	$^{207}Pb/^{235}U$	1σ	$^{207}Pb/^{206}Pb$	1σ
Samp GD23												
1	0.0098	0.0003	10.08	0.4010	0.0045	1.13	178	2	191	24	359	284
2	0.0093	0.0001	4.45	0.5207	0.0030	0.57	179	1	185	8	251	96
3	0.0092	0.0001	4.49	0.6241	0.0032	0.52	176	1	191	8	374	97
4	0.0092	0.0001	4.25	0.5651	0.0087	1.54	180	1	184	7	236	86
5	0.0102	0.0002	5.44	0.3756	0.0025	0.67	178	1	199	11	460	121
6	0.0096	0.0001	4.50	0.6011	0.0038	0.63	180	1	188	10	294	112
7	0.0095	0.0003	4.02	0.5738	0.0032	0.56	180	1	183	5	224	67
8	0.0109	0.0002	4.21	0.5341	0.0026	0.49	178	1	179	8	192	106
9	0.0099	0.0002	4.13	0.4877	0.0035	0.71	179	1	182	8	215	97
10	0.0103	0.0003	5.43	0.4689	0.0035	0.75	179	1	182	13	229	155
11	0.0100	0.0003	3.87	0.5959	0.0031	0.52	180	1	185	4	252	53
12	0.0102	0.0001	4.48	0.4905	0.0025	0.51	178	1	178	9	178	111
13	0.0136	0.0001	5.04	0.5608	0.0034	0.60	177	2	187	11	316	138
14	0.0105	0.0004	3.95	0.5753	0.0033	0.57	178	1	191	5	352	64

Table 1 (continued)

Spot	$^{208}Pb/^{232}Th$	1σ	err%	$^{232}Th/^{238}U$	1σ	err%	$^{206}Pb/^{238}U$ (age)	1σ	$^{207}Pb/^{235}U$	1σ	$^{207}Pb/^{206}Pb$	1σ
15	0.0109	0.0001	4.27	0.4672	0.0100	2.14	177	1	197	6	445	69
16	0.0101	0.0003	4.52	0.5015	0.0025	0.49	177	1	196	11	432	124
17	0.0100	0.0003	4.99	0.6314	0.0037	0.58	177	1	200	13	483	142
18	0.0099	0.0003	4.40	0.4920	0.0024	0.49	180	1	183	8	219	103
19	0.0099	0.0004	3.83	0.5710	0.0037	0.64	177	1	180	3	225	40
20	0.0102	0.0003	4.56	0.6551	0.0039	0.59	177	1	179	12	207	162
21	0.0094	0.0003	4.04	0.6236	0.0031	0.49	179	1	187	8	301	92
22	0.0093	0.0003	4.96	0.6468	0.0036	0.55	181	1	181	20	180	271
23	0.0083	0.0003	6.73	0.4899	0.0025	0.51	178	1	191	22	345	259
24	0.0106	0.0003	5.05	0.6410	0.0034	0.53	176	1	178	10	199	127
25	0.0088	0.0003	3.98	0.5487	0.0040	0.73	180	1	183	4	222	52
26	0.0093	0.0004	4.67	0.4687	0.0061	1.30	179	1	181	11	209	140
27	0.0094	0.0003	5.60	0.5286	0.0044	0.83	177	1	184	15	276	192
28	0.0086	0.0003	4.75	0.5303	0.0043	0.81	178	1	181	11	217	134
29	0.0091	0.0003	4.00	0.5438	0.0029	0.54	178	1	179	6	196	72
30	0.0100	0.0003	11.40	0.5627	0.0027	0.48	177	2	193	18	395	156

Spot	Pb (ppm)	U (ppm)	$^{206}Pb/^{238}U$	1σ	err%	$^{207}Pb/^{235}U$	1σ	err%	$^{207}Pb/^{206}Pb$	1σ	err%
Sample GD1											
1	3	82	0.0276	0.0002	0.84	0.2054	0.0165	8.04	0.0539	0.0041	7.63
2	2	58	0.0276	0.0002	0.85	0.2159	0.0188	8.72	0.0568	0.0050	8.89
3	2	64	0.0278	0.0002	0.75	0.2050	0.0177	8.64	0.0535	0.0046	8.68
4	6	194	0.0280	0.0002	0.66	0.2138	0.0094	4.41	0.0554	0.0024	4.34
5	1	35	0.0281	0.0003	1.24	0.1953	0.0666	34.07	0.0504	0.0216	42.78
6	3	103	0.0280	0.0002	0.73	0.1923	0.0131	6.81	0.0499	0.0034	6.77
7	2	84	0.0279	0.0002	0.68	0.2049	0.0119	5.81	0.0532	0.0031	5.80
8	3	90	0.0282	0.0002	0.80	0.1969	0.0190	9.65	0.0506	0.0049	9.61
9	2	57	0.0282	0.0002	0.86	0.1986	0.0333	16.78	0.0510	0.0088	17.19
10	1	30	0.0278	0.0004	1.27	0.1915	0.0346	18.04	0.0500	0.0100	19.92
11	1	28	0.0280	0.0007	2.32	0.2046	0.0711	34.73	0.0529	0.0227	42.87
12	1	42	0.0277	0.0003	1.15	0.2667	0.0337	12.64	0.0698	0.0088	12.65
13	4	125	0.0275	0.0002	0.68	0.2058	0.0100	4.87	0.0543	0.0026	4.84
14	1	36	0.0283	0.0004	1.59	0.1954	0.0856	43.81	0.0501	0.0282	56.42
15	7	218	0.0278	0.0002	0.62	0.2040	0.0061	3.01	0.0532	0.0016	2.95
16	2	53	0.0283	0.0003	0.97	0.2023	0.0505	24.97	0.0518	0.0138	26.57
17	7	223	0.0277	0.0002	0.60	0.2066	0.0057	2.74	0.0540	0.0015	2.72
18	1	31	0.0274	0.0004	1.41	0.2589	0.0317	12.24	0.0685	0.0085	12.47
19	6	206	0.0277	0.0002	0.61	0.2082	0.0054	2.61	0.0545	0.0014	2.59
20	1	34	0.0281	0.0003	1.17	0.1961	0.0462	23.57	0.0507	0.0147	29.10
21	1	44	0.0284	0.0003	0.96	0.1973	0.0397	20.12	0.0504	0.0111	22.02
22	3	117	0.0277	0.0002	0.72	0.1992	0.0164	8.24	0.0521	0.0043	8.29
23	6	202	0.0280	0.0002	0.60	0.2333	0.0069	2.94	0.0604	0.0018	2.93
24	4	143	0.0275	0.0002	0.64	0.2308	0.0079	3.42	0.0609	0.0021	3.40
25	3	81	0.0280	0.0002	0.74	0.2292	0.0163	7.13	0.0593	0.0042	7.13
26	2	67	0.0277	0.0002	0.74	0.2156	0.0141	6.53	0.0564	0.0037	6.50
27	3	102	0.0277	0.0002	0.65	0.2105	0.0105	4.97	0.0551	0.0027	4.94
28	3	104	0.0278	0.0002	0.64	0.2404	0.0107	4.45	0.0628	0.0028	4.42
29	2	68	0.0277	0.0002	0.74	0.1911	0.0160	8.38	0.0500	0.0042	8.41
30	3	87	0.0278	0.0002	0.67	0.1919	0.0118	6.12	0.0501	0.0031	6.16

Table 1 (continued)

Spot	$^{208}Pb/^{232}Th$	1σ	err%	$^{232}Th/^{238}U$	1σ	err%	$^{206}Pb/^{238}U$ (age)	1σ	$^{207}Pb/^{235}U$	1σ	$^{207}Pb/^{206}Pb$	1σ
Sample GD1												
1	0.0127	0.0003	5.11	0.5231	0.0029	0.56	176	1	190	15	368	172
2	0.0141	0.0001	6.87	0.3504	0.0020	0.58	175	1	198	17	484	196
3	0.0122	0.0001	5.06	0.5214	0.0025	0.47	177	1	189	16	350	196
4	0.0125	0.0001	4.25	0.4099	0.0020	0.48	178	1	197	9	428	97
5	0.0123	0.0002	10.69	0.3688	0.0019	0.51	179	2	181	62	214	991
6	0.0114	0.0001	5.52	0.3946	0.0025	0.64	178	1	179	12	190	158
7	0.0107	0.0003	5.73	0.3329	0.0016	0.49	178	1	189	11	336	131
8	0.0104	0.0002	4.77	0.6131	0.0030	0.49	179	1	182	18	223	222
9	0.0081	0.0002	6.47	0.5663	0.0028	0.49	180	2	184	31	240	396
10	0.0110	0.0003	10.94	0.4064	0.0021	0.51	177	2	178	32	194	463
11	0.0070	0.0003	18.64	0.6425	0.0037	0.57	178	4	189	66	327	973
12	0.0104	0.0001	10.74	0.4577	0.0023	0.50	176	2	240	30	921	260
13	0.0099	0.0001	4.19	0.7902	0.0042	0.53	175	1	190	9	385	109
14	0.0113	0.0004	11.14	0.3813	0.0020	0.53	180	3	181	79	197	1311
15	0.0111	0.0001	3.88	0.6441	0.0041	0.63	177	1	189	6	337	67
16	0.0108	0.0003	5.79	0.6340	0.0044	0.69	180	2	187	47	275	609
17	0.0100	0.0003	3.84	0.8374	0.0043	0.52	176	1	191	5	372	61
18	0.0108	0.0003	13.21	0.4096	0.0022	0.53	174	2	234	29	883	258
19	0.0095	0.0004	3.94	0.6080	0.0083	1.37	176	1	192	5	392	58
20	0.0087	0.0003	11.26	0.4138	0.0021	0.51	178	2	182	43	227	672
21	0.0094	0.0003	6.86	0.5422	0.0028	0.52	180	2	183	37	215	510
22	0.0094	0.0003	5.14	0.5085	0.0039	0.76	176	1	184	15	291	189
23	0.0091	0.0003	3.84	0.7969	0.0039	0.49	178	1	213	6	619	63
24	0.0091	0.0003	4.07	0.7778	0.0037	0.47	175	1	211	7	635	73
25	0.0094	0.0003	4.65	0.6871	0.0033	0.49	178	1	210	15	579	155
26	0.0113	0.0004	5.44	0.5489	0.0094	1.70	176	1	198	13	469	144
27	0.0101	0.0003	4.24	0.6459	0.0031	0.48	176	1	194	10	417	110
28	0.0102	0.0003	4.33	0.6813	0.0035	0.52	177	1	219	10	700	94
29	0.0099	0.0003	5.74	0.4198	0.0020	0.48	176	1	178	15	197	195
30	0.0107	0.0003	4.64	0.4566	0.0022	0.48	177	1	178	11	201	143

pluton shows relatively low SiO_2 composition in a range of 47.09 to 57.15 wt%. Their K_2O and Na_2O contents vary from 0.29 to 1.13 and 1.19 to 3.92 wt%, respectively. The samples form a fairly narrow dispersion in the total alkali versus silica diagram (TAS) and plot in the gabbro and gabbroic diorite, which are consistent with the classifications performed by observing hand specimens and microscopy (Fig. 4). All the rocks were mostly metaluminous with A/CNK ratios (molar $Al_2O_3/[CaO + Na_2O + K_2O]$) ranging from 0.64 to 0.97 (Fig. 5a, b) and usually plot in the calc-alkaline field of the TAS diagram (Fig. 5c). According to their A/NK and A/CNK ratios, these rocks can be classified as I-type affinity (Fig. 5b). These rocks were characterized by relatively high MgO (2.55–9.43 wt%), Al_2O_3 (14.36–23.03 wt%), $Fe_2O_3^{tot}$ (5.45–11.12 wt%) concentrations and Mg# values $[(100 \times MgO/(MgO + 0.9Fe_2O_3^{tot})]$

varying from 46 to 75. The transition metals concentrations of the samples were lower than those of primitive mafic magmas (Frey et al. 1978), suggesting the more differentiated nature of the former. It is apparent that all the rocks generally exhibit positive correlations between SiO_2 and A/CNK, while they have a negative correlation between A/CNK and A/NK molar ratio (Fig. 5a, b).

Trace elements

The trace-element concentrations are provided in Table 2. The gabbroic rocks from the pluton had variable content of total REEs. The samples were characterized by low Yb concentrations (0.74 to 4.36 ppm) and slightly positive and negative or no Eu anomalies with a Eu/Eu* range of 0.61 to 1.62, which likely reflects fractionation

Table 2 Major oxide (wt%) and trace-element (ppm) compositions of the calc-alkaline Gokcedere gabbroic pluton in the eastern Sakarya Zone

Sample	GD1	GD2	GD6	GD7	GD9	GD10	GD12	GD13
Coordinates	37T 566892 E 4440228N	37T 566744 E 4439743N	37T 566011 E 4439085N	37T 565868 E 4438358N	37T 565752 E 4437708N	37T 566430 E 4437878N	37T 567047 E 4438589N	37T 567640 E 4439058N
Rock type	gbb	gbb	gbb	gbb	gbb	gbb	gbb dio	gbb
SiO_2	48.39	51.34	52.23	51.42	52.19	52.14	54.24	51.57
TiO_2	0.92	0.60	0.48	0.68	0.88	0.64	0.26	0.61
Al_2O_3	18.78	17.61	17.38	19.27	18.83	20.79	16.32	23.03
$Fe_2O_3^{tot}$	11.12	7.76	7.67	8.26	9.74	7.51	5.96	5.98
MnO	0.15	0.15	0.15	0.16	0.18	0.12	0.14	0.09
MgO	5.32	6.78	6.93	4.94	4.47	3.75	7.55	2.55
CaO	11.08	10.19	10.43	7.94	8.81	9.83	10.45	10.91
Na_2O	2.24	2.94	2.61	3.92	3.31	3.10	2.42	2.76
K_2O	0.35	0.46	0.48	0.76	0.47	0.44	0.48	0.67
P_2O_5	0.05	0.02	0.03	0.07	0.09	0.03	0.03	0.04
Cr_2O_3	0.01	0.02	0.01	0.01	0.00	0.01	0.02	0.00
LOI	1.40	2.00	1.50	2.40	0.90	1.50	2.00	1.60
Total	99.81	99.85	99.87	99.86	99.86	99.85	99.90	99.87
Mg#	49	63	64	54	48	50	72	46
ASI	0.78	0.74	0.73	0.89	0.86	0.89	0.69	0.92
Rb	6.20	9.30	9.50	18.80	7.70	6.60	12.80	13.50
Sr	182.80	211.80	179.80	275.90	208.10	202.70	151.00	220.80
Ba	109	150	119	133	111	136	123	120
Cs	0.40	0.50	0.60	1.00	0.20	0.20	5.10	0.50
Zr	40.50	121.20	34.80	28.30	32.60	29.60	36.20	36.10
Hf	1.40	2.90	1.00	0.80	0.80	0.90	1.10	1.20
Th	0.70	2.60	<0.2	1.10	0.50	0.70	1.50	1.40
Pb	0.90	0.60	0.60	1.20	0.60	1.00	0.80	1.90
Zn	19	16	10	39	24	23	11	18
Ta	0.10	0.10	0.10	0.10	0.10	0.10	0.10	0.20
Nb	1.10	0.90	0.90	1.30	1.30	0.60	0.60	1.30
Y	23.20	30.60	18.70	13.50	17.70	9.30	12.90	10.10
U	0.1	0.30	0.1	0.1	0.1	0.1	0.10	0.20
Ni	<20	<20	<20	<20	<20	<20	<20	<20
Co	31.80	26.70	26.70	22.50	24.40	23.00	25.10	14.00
V	571	249	212	238	309	412	120	221
Ga	17.10	13.60	14.20	16.10	17.00	16.20	10.30	17.20
Sc	40	48	36	26	35	28	38	20
La	3.90	4.50	3.30	4.60	4.40	3.40	3.90	4.40
Ce	9.80	9.80	8.90	10.40	9.10	6.20	7.60	8.60
Pr	1.37	1.45	1.20	1.27	1.19	0.71	0.92	1.00
Nd	6.50	7.80	5.90	6.60	6.10	3.20	4.50	3.60
Sm	2.41	2.82	1.71	1.66	1.86	0.80	1.37	1.09
Eu	0.66	0.81	0.61	0.74	0.78	0.57	0.41	0.65
Gd	3.15	4.32	2.59	1.99	2.50	1.46	1.80	1.52
Tb	0.59	0.73	0.46	0.37	0.42	0.24	0.31	0.24
Dy	4.23	4.98	3.54	2.23	2.86	1.59	2.56	1.72
Ho	0.88	1.16	0.68	0.50	0.66	0.35	0.48	0.33
Er	2.62	3.44	2.12	1.56	1.74	0.99	1.33	1.12
Tm	0.38	0.49	0.32	0.21	0.27	0.15	0.22	0.16
Yb	2.63	2.91	2.38	1.55	1.58	0.94	1.43	1.10

Table 2 (continued)

Sample	GD1	GD2	GD6	GD7	GD9	GD10	GD12	GD13
Coordinates	37T 566892 E 4440228N	37T 566744 E 4439743N	37T 566011 E 4439085N	37T 565868 E 4438358N	37T 565752 E 4437708N	37T 566430 E 4437878N	37T 567047 E 4438589N	37T 567640 E 4439058N
Rock type	gbb	gbb	gbb	gbb	gbb	gbb	gbb dio	gbb
Lu	0.38	0.49	0.35	0.22	0.30	0.16	0.23	0.16
(La/Yb)n	1.48	1.55	1.39	2.97	2.78	3.62	2.73	4.00
(Eu/Eu*)	0.73	0.71	0.89	1.25	1.11	1.62	0.80	1.55
T_{Zr} (°C)	603	673	594	605	611	609	595	624

Sample	GD14	GD16	GD17	GD18	GD19	GD21	GD22	GD23
Coordinates	37T 567939 E 4439510N	37T 568962 E 4439713N	37T 568567 E 4440080N	37T 567952 E 4440193N	37T 568544 E 4440997N	37T 568756 E 4440872N	37T 569438 E 4440528N	37T 570038 E 4440368N
Rock type	gbb	gbb	gbb dio	gbb dio	gbb	gbb dio	gbb dio	gbb dio
SiO_2	51.24	48.13	54.60	57.15	47.09	54.82	53.65	52.66
TiO_2	0.53	0.39	0.54	0.44	0.21	0.73	0.65	0.53
Al_2O_3	21.03	17.66	14.36	16.26	20.59	15.36	18.47	18.57
$Fe_2O_3^{tot}$	6.44	7.45	6.90	5.47	5.45	10.11	8.20	7.31
MnO	0.12	0.16	0.15	0.12	0.11	0.19	0.14	0.14
MgO	4.65	9.43	8.54	5.93	8.19	6.03	4.93	5.33
CaO	11.51	12.40	9.06	7.96	14.46	7.99	6.98	9.18
Na_2O	2.49	1.65	3.15	3.86	1.19	2.55	3.54	3.19
K_2O	0.30	0.29	0.65	0.71	0.25	0.67	0.96	0.55
P_2O_5	0.03	0.04	0.05	0.11	0.02	0.10	0.05	0.08
Cr_2O_3	0.01	0.02	0.13	0.02	0.03	0.02	0.00	0.01
LOI	1.50	2.30	1.70	1.80	2.30	1.30	2.30	2.30
Total	99.89	99.89	99.86	99.88	99.91	99.85	99.85	99.87
Mg#	59	71	71	68	75	54	54	59
ASI	0.83	0.69	0.64	0.75	0.72	0.79	0.94	0.82
Rb	3.50	7.90	16.90	14.70	8.00	16.80	24.90	12.20
Sr	197.20	170.10	166.00	169.40	162.40	147.20	222.00	188.90
Ba	76	66	130	127	40	146	202	116
Cs	0.10	1.10	0.50	0.60	4.10	0.30	0.80	0.50
Zr	26.30	20.70	73.60	125.50	17.20	92.50	37.10	58.30
Hf	1.00	0.60	2.50	3.10	0.40	3.00	1.20	1.30
Th	0.80	1.50	0.50	0.90	0.30	2.80	1.20	2.20
Pb	1.50	1.00	0.50	0.60	1.40	1.10	1.00	1.40
Zn	19	21	11	10	23	29	35	28
Ta	0.10	0.10	0.10	0.10	0.10	0.20	0.10	0.30
Nb	0.40	0.40	1.50	1.40	0.60	2.70	1.40	2.50
Y	11.30	11.30	39.30	38.20	7.70	33.50	15.70	15.60
U	0.1	0.10	0.20	0.1	0.1	0.50	0.30	0.50
Ni	21	27	85	23	34	23	23	23
Co	22.20	34.70	27.60	19.00	27.70	28.90	23.80	22.40
V	192	187	203	108	128	277	264	200
Ga	14.40	12.60	12.70	11.50	11.30	15.60	18.40	18.10
Sc	28	46	43	36	40	39	28	28
La	3.40	2.80	6.50	6.80	1.40	9.30	4.30	7.50
Ce	7.20	4.50	17.60	15.10	3.30	22.70	9.40	15.10
Pr	0.84	0.62	2.67	2.18	0.41	3.07	1.22	1.80
Nd	4.10	3.20	12.50	11.60	2.30	14.70	6.30	7.50
Sm	1.08	1.19	4.04	3.70	0.71	4.11	1.54	1.84

Table 2 (continued)

Sample	GD14	GD16	GD17	GD18	GD19	GD21	GD22	GD23
Coordinates	37T 567939 E 4439510N	37T 568962 E 4439713N	37T 568567 E 4440080N	37T 567952 E 4440193N	37T 568544 E 4440997N	37T 568756 E 4440872N	37T 569438 E 4440528N	37T 570038 E 4440368N
Rock type	gbb	gbb	gbb dio	gbb dio	gbb	gbb dio	gbb dio	gbb dio
Eu	0.54	0.39	0.98	0.90	0.27	0.97	0.58	0.70
Gd	1.67	1.60	5.19	5.53	1.04	5.08	2.28	2.56
Tb	0.27	0.29	0.88	0.95	0.18	0.83	0.37	0.40
Dy	1.89	1.75	5.99	6.46	1.29	5.93	2.69	2.82
Ho	0.42	0.39	1.37	1.46	0.28	1.24	0.59	0.59
Er	1.23	1.28	4.41	3.99	0.77	3.46	1.57	1.71
Tm	0.18	0.19	0.62	0.59	0.12	0.54	0.25	0.28
Yb	1.21	1.15	4.36	3.92	0.74	3.50	1.71	1.55
Lu	0.19	0.16	0.66	0.61	0.12	0.55	0.27	0.26
(La/Yb)n	2.81	2.43	1.49	1.73	1.89	2.66	2.51	4.84
(Eu/Eu*)	1.23	0.87	0.66	0.61	0.96	0.65	0.95	0.99
T_{Zr} (°C)	592	546	626	694	540	676	635	644

Sample	GD24	GD28	GD30	GD41
Coordinates	37T 570478 E 4440599N	37T 570721 E 4441140N	37T 569486 E 4441576N	37T 570123 E 4441788N
Rock type	gbb dio	gbb	gbb dio	gbb
SiO_2	53.26	51.59	53.90	51.30
TiO_2	0.67	0.64	0.63	0.59
Al_2O_3	18.49	18.92	18.63	18.50
$Fe_2O_3^{tot}$	8.04	8.23	7.98	8.72
MnO	0.15	0.16	0.15	0.17
MgO	4.69	5.42	4.70	5.96
CaO	7.77	9.44	6.33	9.36
Na_2O	3.22	2.37	3.89	2.59
K_2O	0.71	0.77	1.13	0.53
P_2O_5	0.06	0.06	0.05	0.06
Cr_2O_3	0.01	0.01	0.01	0.01
LOI	2.80	2.30	2.50	2.10
Total	99.86	99.87	99.85	99.85
Mg#	54	57	54	58
ASI	0.92	0.86	0.97	0.85
Rb	17.60	21.90	29.40	12.90
Sr	227.40	179.80	251.60	228.10
Ba	137	154	199	160
Cs	0.50	0.60	1.20	0.30
Zr	48.60	30.40	47.80	30.60
Hf	1.40	1.20	1.70	1.30
Th	1.40	1.30	1.10	1.00
Pb	1.00	0.90	1.50	1.10
Zn	37.00	26.00	39.00	27.00
Ta	0.20	0.20	0.10	0.10
Nb	2.40	2.10	1.20	1.90
Y	15.40	15.30	14.60	15.60
U	0.20	0.1	0.20	0.1
Ni	21	30	22	51
Co	21.50	22.90	22.60	27.90

Table 2 (continued)

Sample	GD24	GD28	GD30	GD41
Coordinates	37T 570478 E 4440599N	37T 570721 E 4441140N	37T 569486 E 4441576N	37T 570123 E 4441788N
Rock type	gbb dio	gbb	gbb dio	gbb
V	224	225	243	327
Ga	16.80	15.90	15.90	18.50
Sc	27.00	30.00	27.00	35.00
La	5.50	5.60	4.00	4.60
Ce	11.30	11.60	8.50	9.70
Pr	1.50	1.54	1.10	1.23
Nd	6.50	6.40	4.40	7.10
Sm	1.74	1.70	1.42	1.91
Eu	0.66	0.59	0.61	0.69
Gd	2.19	2.32	2.08	2.27
Tb	0.39	0.35	0.37	0.41
Dy	2.92	2.60	2.26	2.78
Ho	0.58	0.49	0.53	0.61
Er	1.53	1.53	1.56	1.73
Tm	0.23	0.24	0.24	0.27
Yb	1.67	1.84	1.77	1.69
Lu	0.25	0.26	0.26	0.30
(La/Yb)n	3.29	3.04	2.26	2.72
(Eu/Eu*)	1.04	0.91	1.09	1.02
T_{Zr} (°C)	649	608	655	605

Rock types: *gbb* gabbro. *gbb.dio* gabbroic diorite. LOI: loss on ignition. Mg# is $100 \times MgO/(MgO + 0.9FeO_{tot})$ in molar proportions. Oxides are given in wt%. trace elements in µg/g (ppm). ASI is the aluminium saturation index [molar $Al_2O_3/(CaO + K_2O + Na_2O)$]. $T_{Zr}(^0C)$: whole-rock Zr saturation temperature was estimated using the Zr solubility in granitic melts (Watson and Harrison 1983)

Fig. 4 Rock classification diagram (Middlemost 1994) for the Gokcedere pluton. σ is a Rittmann index, defined as $(K_2O + Na_2O)^2/(SiO_2 - 43)$
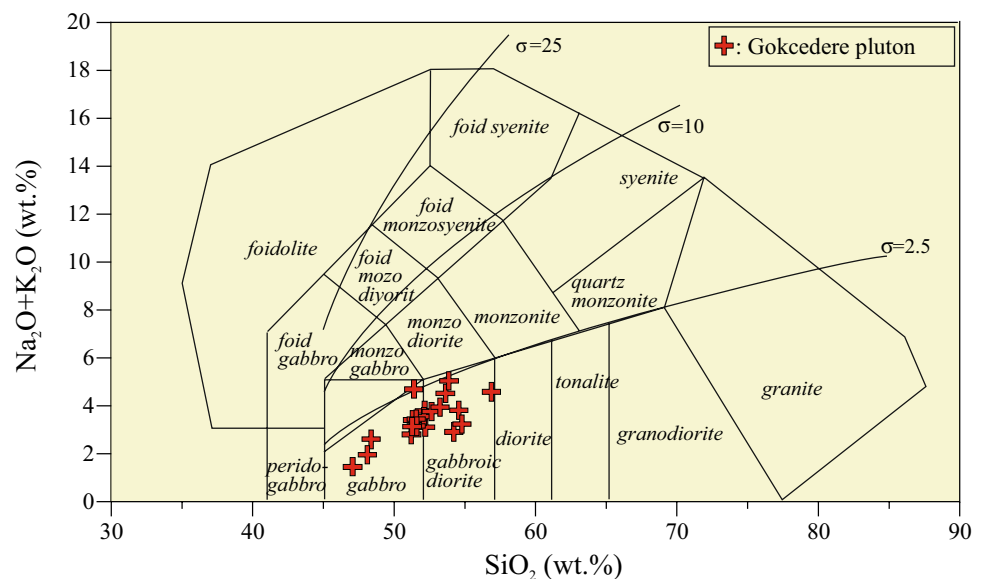
or accumulation of plagioclase. Based on the chondrite-normalized REE patterns of the intrusive rocks, all the samples displayed slight LREEs fractionation patterns and a nearly flat HREE slope with (La/Yb)n varying from 1.39 to 4.84 (Fig. 6a). All the samples exhibited similar patterns, namely enrichment in large ion lithophile
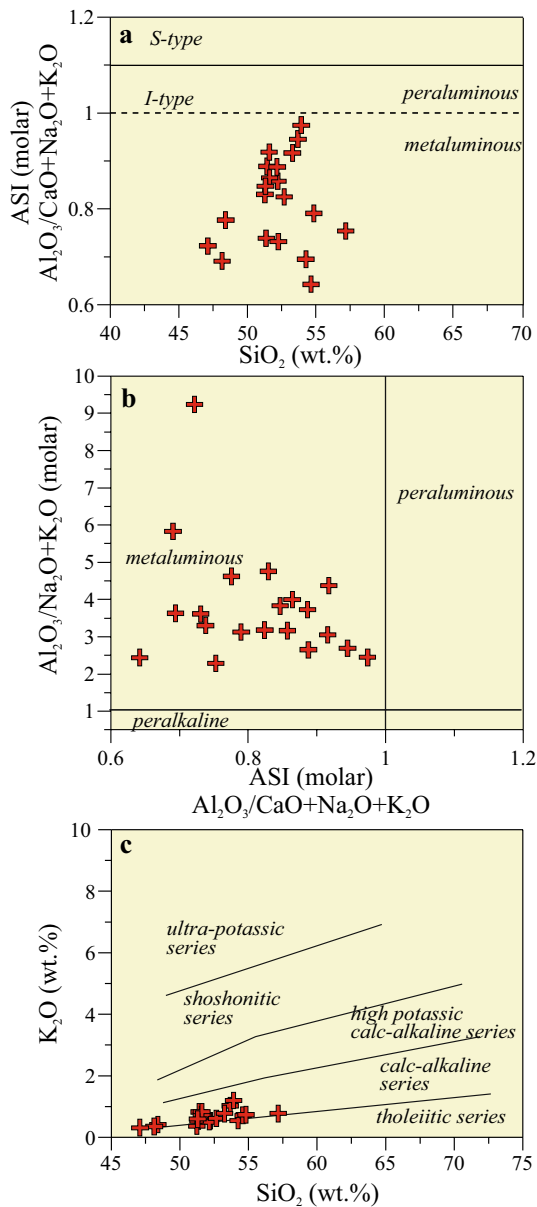
Fig. 5 a ASI versus SiO_2, **b** $Al_2O_3/Na_2O + K_2O$ (molar) versus ASI [after Maniar and Piccoli (1989)], **c** K_2O versus SiO_2 [after Peccerillo and Taylor (1976)] for the samples from the Gokcedere gabbroic samples

Fig. 6 a Chondrite values [normalized to values taken from Boynton (1984)] of rare-earth element abundance patterns for the selected samples from the studied plutons. **b** PM-normalized multi-element variation patterns [normalized to values taken from Sun and McDonough (1989)] for the calc-alkaline gabbroic pluton

elements (LILEs) (Ba, Rb, Th, and K) relative to high field strength elements (HFSEs), with marked negative Nb and Ti anomalies and no depletion of Hf and Zr in the primitive mantle normalized multiple-element variation diagrams (Fig. 6b). The positive Eu and Sr anomalies of some samples are indicative of some degree of plagioclase accumulation in the generation. The gabbroic samples of the pluton had low and variable Ni (<20 to 85 ppm) and Co (14 to 35 ppm) content.

In situ zircon Lu-Hf isotope systematic

The 19 Hf isotopic spots of 25 zircons from sample GD1 and 16 Hf isotopic spots of 20 zircons from sample GD23 of the pluton were analyzed at the same sites as those used for U–Pb dating. Table 3 exhibits in situ zircon Lu-Hf isotope data of the gabbroic samples. The zircon U–Pb ages were used for all the zircon grains to recalculate $\varepsilon_{Hf}(t)$ and T_{DM1} values. The $^{176}Lu/^{177}Hf$ ratios were close to 0.001, suggesting no significant accumulation of radiogenic Hf after zircon crystallization. Based on the CL images of the zircons, measured $^{176}Hf/^{177}Hf$ ratios revealed the composition of the Hf isotope system at the time of zircon crystallization (Wu et al. 2007). The spots are generally plotted above the CHUR evolutionary line in the diagram of $\varepsilon_{Hf}(t)$ versus age (Ma) (Fig. 7). The $\varepsilon_{Hf}(t)$ values of the zircons of samples GD1 and GD23 from the pluton were variable and positive and in the range of 4.6–13.5, varying over a total range of 8.9 ε_{Hf} units and an average value of 8.3, which corresponds to T_{DM1} model ages of 0.30 to 0.65 Ga for the Gokcedere gabbroic pluton.

Whole-rock Sr-Nd isotopic compositions

Table 4 shows the results of five analyses for Sr and Nd isotopic ratios from the Gokcedere gabbroic pluton, Demirozu-Bayburt area, northeast Turkey. The measured isotope ratios of the samples were corrected by an average age of

177 Ma based on the U–Pb zircon age technique. The gabbroic rocks had nearly homogenous and relatively depleted isotopic compositions, with $(^{87}Sr/^{86}Sr)_i$ of 0.705124 to 0.705599 and ε_{Nd} (t) of 0.1 to 3.5. The single-stage Nd model ages (T_{DM1}) relative to a depleted mantle reservoir were relatively young, and the values ranged from 0.65 to

Table 3 In situ zircon Hf isotopic data of the calc-alkaline Gokcedere gabbroic pluton from the Bayburt area in the eastern Sakarya Zone

Sample/spot	176Yb/177Hf	176Lu/177Hf	176Hf/177Hf	2σ	Age (Ma)	εHf(t)	fLu/Hf	TDM1(Ga)
GD1-1	0.034516	0.001107	0.282964	0.000019	176	10.6	−0.97	0.41
GD1-2	0.028906	0.000992	0.282929	0.000018	176	9.3	−0.97	0.46
GD1-3	0.029783	0.000954	0.282935	0.000020	176	9.5	−0.97	0.45
GD1-4	0.027558	0.000952	0.282902	0.000020	176	8.4	−0.97	0.50
GD1-5	0.031469	0.001066	0.282899	0.000020	176	8.3	−0.97	0.50
GD1-6	0.045283	0.001449	0.282945	0.000020	176	9.9	−0.96	0.44
GD1-7	0.051560	0.001792	0.282902	0.000018	176	8.3	−0.95	0.51
GD1-8	0.028481	0.000925	0.282894	0.000021	176	8.1	−0.97	0.51
GD1-9	0.041750	0.001375	0.282961	0.000017	176	10.4	−0.96	0.42
GD1-10	0.034021	0.001227	0.282895	0.000020	176	8.1	−0.96	0.51
GD1-11	0.040115	0.001310	0.282981	0.000021	176	11.1	−0.96	0.39
GD1-12	0.058677	0.001919	0.283050	0.000019	176	13.5	−0.94	0.29
GD1-13	0.023249	0.000817	0.282968	0.000019	176	10.7	−0.98	0.40
GD1-14	0.038196	0.001289	0.282948	0.000019	176	9.9	−0.96	0.44
GD1-15	0.051714	0.001724	0.282907	0.000020	176	8.5	−0.95	0.50
GD1-16	0.054535	0.001809	0.282979	0.000018	176	11.0	−0.95	0.40
GD1-17	0.053749	0.001870	0.282980	0.000020	176	11.0	−0.94	0.40
GD1-18	0.029319	0.000974	0.282927	0.000018	176	9.3	−0.97	0.46
GD1-19	0.028267	0.001003	0.282944	0.000018	176	9.8	−0.97	0.44
Sample/Spot	176Yb/177Hf	176Lu/177Hf	176Hf/177Hf	2σ	Age (Ma)	εHf(t)	fLu/Hf	TDM1(Ga)
GD23-1	0.028722	0.000967	0.282797	0.000018	178	4.7	−0.97	0.65
GD23-2	0.050720	0.001680	0.282834	0.000021	178	5.9	−0.95	0.61
GD23-3	0.025657	0.000924	0.282896	0.000021	178	8.2	−0.97	0.51
GD23-4	0.041282	0.001354	0.282829	0.000017	178	5.8	−0.96	0.61
GD23-5	0.037532	0.001298	0.282884	0.000020	178	7.7	−0.96	0.51
GD23-6	0.076196	0.002493	0.282890	0.000020	178	7.8	−0.92	0.54
GD23-7	0.037834	0.001260	0.282840	0.000018	178	6.2	−0.96	0.59
GD23-8	0.030632	0.001057	0.282800	0.000019	178	4.8	−0.97	0.64
GD23-9	0.027348	0.000965	0.282824	0.000018	178	5.6	−0.97	0.61
GD23-10	0.051408	0.001685	0.282859	0.000021	178	6.8	−0.95	0.57
GD23-11	0.038873	0.001302	0.282934	0.000020	178	9.5	−0.96	0.46
GD23-12	0.034693	0.001153	0.282824	0.000019	178	5.6	−0.97	0.61
GD23-13	0.030601	0.001078	0.282867	0.000018	178	7.1	−0.97	0.55
GD23-14	0.030369	0.001035	0.282842	0.000016	178	6.3	−0.97	0.58
GD23-15	0.024973	0.000966	0.282796	0.000019	178	4.6	−0.97	0.65
GD23-16	0.028376	0.000966	0.282842	0.000018	178	6.3	−0.97	0.58

$\varepsilon_{Hf}(0) = ((^{176}Hf/^{177}Hf)_S/(^{176}Hf/^{177}Hf)_{CHUR,0} - 1) \times 10{,}000$, $f_{Lu/Hf} = (^{176}Lu/^{177}Hf)_S/(^{176}Lu/^{177}Hf)_{CHUR} - 1$

$\varepsilon_{Hf}(t) = ((^{176}Hf/^{177}Hf)_S - (^{176}Lu/^{177}Hf)_S \times (e^{\lambda t} - 1))/((^{176}Hf/^{177}Hf)_{CHUR} - (^{176}Lu/^{177}Hf)_{CHUR} \times (e^{\lambda t} - 1)) - 1) \times 10{,}000$

$T_{DM1}(Hf) = 1/l \times (1 + ((^{176}Hf/^{177}Hf)_S - (^{176}Hf/^{177}Hf)_{DM})/((^{176}Lu/^{177}Hf)_S - (^{176}Lu/^{177}Hf)_{DM}))$

$(^{176}Hf/^{177}Hf)_S$ measured values; $(^{176}Lu/^{177}Hf)_{CHUR} = 0.0332$, $(^{176}Hf/^{177}Hf)_{CHUR,0} = 0.282772$ (Blichert-Toft and Albarède 1997)

$(^{176}Lu/^{177}Hf)_{DM} = 0.0384$ ve $(^{176}Hf/^{177}Hf)_{DM} = 0.28325$ (Griffin et al. 2000); $f_{CC} = -0.548$ (composition of continental crust), $f_{DM} = 0.16$, $t =$ zircon crystallization time, $\lambda = 1.865 \times 10^{-11} year^{-1}$ calculations based on (Söderlund et al. 2004)

0.95 Ga. The data are illustrated in a plot of $(^{87}Sr/^{86}Sr)_i$ versus ε_{Nd} (t) in Fig. 8, and compared on the diagram with the reference compositional field previously published for the area. Their Sr-Nd isotopic values plot in proximity to the compositional fields of hybrid granitoids from the Eastern Pontides (Karsli et al. 2007), subduction-related plagioleucitites (Altherr et al. 2008), and middle Eocene shoshonitic granitoids (Karsli et al. 2012b) and are far from the compositional ranges of late Carboniferous to early Permian plutons (Karsli et al. 2016), hybrid Harsit pluton (Karsli et al. 2010a), and A-type granites from the Eastern Pontides (Karsli et al. 2012a) (Fig. 8).

Zircon saturation thermometry

Whole-rock Zr saturation temperatures (T_{Zr}) were estimated using the Zr solubility in granitic melts (Watson and Harrison 1983). If a granitic melt is saturated with Zr, its temperature can be calculated from the measured major element and Zr content. The results for the gabbroic samples are reported in Table 2. The zircon saturation temperature (T_{Zr}) values of the present samples were in the range of 540–694 °C (average of 619 °C, Table 2), which are lower than those of A-type magmas. Considering CL images and U–Pb ages (Fig. 3; Table 1), the Gokcedere pluton does not have zircon inheritance, suggesting that zircons in the pluton were in near-liquid phases, which was mirrored by the euhedral form of the zircons. Miller et al. (2003) stated that T_{Zr} provides a good estimate of magma temperature in the case of inheritance-poor (<10% grains with premagmatic cores) granitoids. Therefore, the calculated T_{Zr} values for the pluton are approximate to their magma temperature.

Discussion

Emplacement age of the Gokcedere gabbroic pluton

Zircon is a resistant mineral, with the highest closure temperature, and has strong resistance to overprinting geological processes. Thus, records of magma crystallization can be preserved in the growths of zircon domains. Prior to this study, Dokuz et al. (2006, 2010) and Karsli et al. (2014) proposed that sporadic magmatism occurred in the late Triassic to early Jurassic in response to the subduction of Paleo-Tethyan oceanic lithosphere. The zircons of this study are of magmatic origin, mimicking their morphology and oscillatory zone textures (Hoskin and Schaltegger 2003). All spots are close to the concordant curve, indicating that the zircon U–Pb isotope system remained largely closed after the crystallization of zircon. We performed LA-ICP-MS zircon U–Pb dating of the gabbroic intrusion in the eastern Sakarya Zone to precisely determine
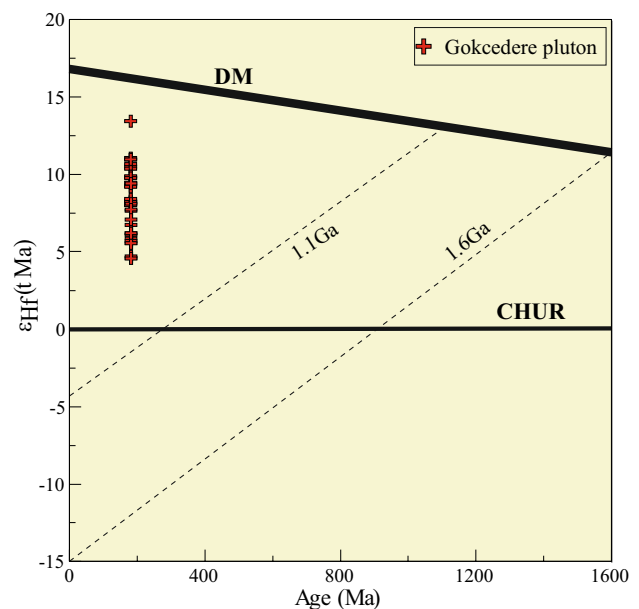
Fig. 7 Correlation diagram of in situ zircon ε_{Hf} (t) values versus U–Pb ages for the Gokcedere pluton in the eastern Sakarya Zone

its geochronological framework. The concordant analyses in this work yielded weighted mean $^{206}Pb/^{238}U$ ages of 176.95 ± 0.49 and 178.41 ± 0.44 Ma, revealing the emplacement age of the pluton (Fig. 3a, b). In contrast to the recent works mentioned above, new zircon U–Pb age data for the gabbroic rocks from the eastern Sakarya Zone demonstrates that the pluton was emplaced at ~177 Ma in the region. The Gokcedere pluton intruded the early Carboniferous Pulur metamorphics and covered by the early to middle Jurassic Şenköy Formation, and our present age data is consistent with those of Pulur metamorphics and the Şenköy Formation reported in Topuz et al. (2004) and Kandemir (2004), respectively. Considering the integrated age data, sporadic magmatic activity occurred in the early Jurassic period, likely indicating late-phase subduction of the Paleo-Tethyan oceanic lithosphere before the Cimmerian Orogeny in the region.

Genetic model of the pluton

In general, the gabbroic to gabbroic diorite samples from the Gokcedere pluton possess low lost on ignition (LOI) values (mostly <2%), suggesting minor or no alteration. Therefore, we can use its major and trace-element composition to constrain the genetic model. Similarities in aspects of the major and trace-element composition of the gabbroic to gabbroic diorite samples point to a shared magmatic origin that is remarkably different from the late Paleozoic widespread magmatism of the region in terms of their geochemical and isotopic signatures. They exhibit A/

Table 4 Whole-rock Sr and Nd isotopic compositions of the calc-alkaline Gokcedere gabbroic pluton in the eastern Sakarya Zone

Sample	[Rb] ppm	[Sr] ppm	$^{87}Rb/^{86}Sr$	$^{87}Sr/^{86}Sr$	2σ m	$(^{87}Sr/^{86}Sr)_i$	[Sm] ppm	[Nd] ppm	$^{147}Sm/^{144}Nd$	$^{143}Nd/^{144}Nd$	2σ m	$\varepsilon_{Nd}(t)$	T_{DM1} (Ga)
Gokcedere Pluton													
GD2	9	212	0.13	0.705862	5	0.705540	2.8	8	0.22	0.512808	6	2.8	0.69
GD12	13	151	0.25	0.706003	4	0.705382	1.4	5	0.18	0.512742	6	2.3	0.74
GD18	15	169	0.25	0.706235	6	0.705599	3.7	12	0.19	0.512784	7	2.9	0.68
GD19	8	162	0.14	0.705485	6	0.705124	0.7	2	0.19	0.512806	8	3.5	0.65
GD23	12	189	0.19	0.705904	7	0.705431	1.8	8	0.15	0.512585	8	0.1	0.95

$\varepsilon_{Nd} = ((^{143}Nd/^{144}Nd)_s/(^{143}Nd/^{144}Nd)_{CHUR} - 1) \times 10{,}000$, $f_{Sm/Nd} = (^{147}Sm/^{144}Sm)_s/(^{147}Sm/^{144}Sm)_{CHUR} - 1$, $(^{143}Nd/^{144}Nd)_{CHUR} = 0.512638$, and $(^{147}Sm/^{144}Sm)_{CHUR} = 0.1967$. The model ages were calculated using a linear isotopic ratio growth equation: $T_{DM1} = 1/\lambda \times \ln(1 + ((^{143}Nd/^{144}Nd)_s - 0.51315)/((^{147}Sm/^{144}Nd)_s - 0.2137))$
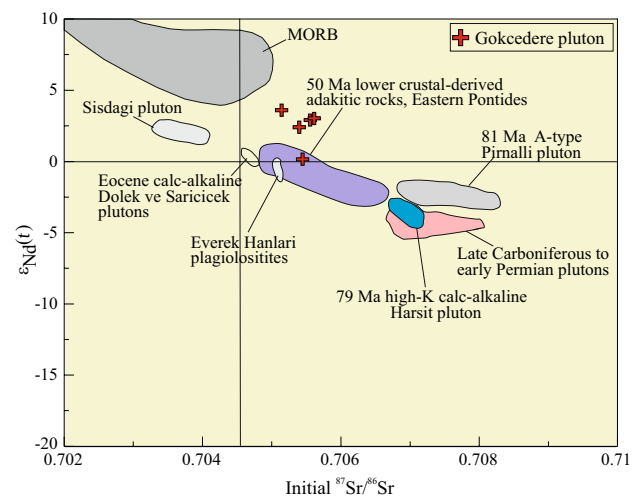
Fig. 8 ε_{Nd} (t) versus $(^{87}Sr/^{86}Sr)_i$ values for the calc-alkaline Gokcedere pluton from the Bayburt region in the eastern Sakarya Zone. Data sources are as follows: 400–179 Ma MORB from Mahoney et al. (1998), Xu et al. (2003), and Tribuzio et al. (2004). Eocene Sisdagi pluton in the region, Paleocene plagioleucitites, and high-K calc-alkaline Harsit rocks are after Karsli et al. 2012b, Altherr et al. (2008), and Karsli et al. (2010a), respectively. Eocene Dolek and Saricicek hybrid plutons are after Karsli et al. (2007). The A-type plutons from the eastern Sakarya Zone are from Karsli et al. (2012a)

CNK <0.97, relatively moderate Na_2O (1.19–3.92 wt%), high Mg# (46–75), and notably low Ni (<85 ppm) and Co (<35 ppm). Such mineralogical and geochemical signatures are clearly indicative of I-type affinity rather than S-type classification. Further, the relatively low T_{Zr} (<695 °C; Table 2) of the samples based on low Zr (ppm) content rules out A-type genesis. Thus, we believe that the Gokcedere pluton are of I-type granitoid. A variety of genetic models have been proposed to constrain the origin of I-type magmas, such as (a) a result of the partial melting of igneous crustal source rocks (Chappell and White 1992), (b) mixing of mantle- and crustal-derived magmas (Castro et al. 1991), and (c) partial melting of the lower crust triggered by the heat coming from basaltic underplated magmas in an extensional phase (Kemp et al. 2005; He et al. 2010).

Differentiation processes

The gabbroic rocks of Gokcedere pluton have relatively lower transition metals than those of primitive basic melts (Frey et al. 1978), suggesting the rocks were derived from relatively evolved magmas. Thus, the low Ni and Co content relative to primitive basic melt is considered to decrease as a consequence of magmatic differentiation. Furthermore, the gabbroic rocks also possess a narrow range of $(^{87}Sr/^{86}Sr)_i$ values (0.705124 to 0.705599) and positive ε_{Nd} (t) values (0.1 to 3.5). The ancient zircon

population are expected for the significant contamination during the magma evolution. However, they were not observed during in situ zircon analysis for the present work. Notably, the depletion of Nb and Ti was expected due to crustal contamination. Rocks related to crustal contamination should exhibit enrichment of Zr and Hf. This is not the case for the Gokcedere gabbroic rocks in the spidergrams (Fig. 6b). Moreover, the gabbroic samples display linear correlations between the major oxides and SiO_2 on Harker variation diagrams (not shown), implicating lithological and geochemical variations of the samples are due to crystal fractionation during magma transport and emplacement. The negative Ba, Sr, and Ti anomalies on the spidergrams of Fig. 6b imply the magmas experienced the fractionation of plagioclase and Fe-Ti oxide, which also supports the above interpretation. Therefore, we propose that the crustal contamination process may be limited or insignificant in the generation and that crystal fractionation played a significant role in the slightly evolved signature of the Gokcedere gabbroic rocks, which formed in the eastern Sakarya Zone in response to slab roll-back of the Paleo-Tethyan oceanic lithosphere in the early Jurassic period before the Cimmerian Orogeny.

Source nature

The gabbroic samples of the early Jurassic Gokcedere pluton were characterized by relatively high Sr (147–222 ppm), high Y (10–39 ppm), and HREE concentrations (Yb = 0.94–4.36 ppm) and low (La/Yb)n (1.39–4.84) values, mimicking geochemical signature comparable to normal island arc-derived rocks (Defant and Drummond 1990). The studied rocks possessed low SiO_2 content (47.09–57.15 wt.7%) and high Mg# values (46–75) and relatively high concentrations of compatible elements (Ni = 20–85 ppm; Co = 14–35). These geochemical features point to a mantle component in their origin. Their moderately fractionated LREE and HREE patterns, enrichment in LREEs relative to HREEs, depletion in HFSEs (such as Nb and Ti), and general lack of Eu anomalies also indicate a subduction signature (e.g., Hawkesworth et al. 1997; Elburg et al. 2002; Cameron et al. 2003). However, all geochemical features of this work reveal that their magmas do not represent their primary nature and that they experienced some crystal fractionation. The mantle origin was confirmed by relatively low ($^{87}Sr/^{86}Sr$)i values (0.705124 to 0.705599) and positive ε_{Nd} (t) values (0.1–3.5), which were close to the MORB area in the Fig. 8. Hf isotopic composition in zircon is an efficient tool to elucidate the nature of magma source and magma mixing processes (e.g., Griffin et al. 2002). Accordingly, igneous rocks having similar U–Pb zircon ages and varying ε_{Hf} (t) values are expected to derive from different source magmas or source

heterogeneity (e.g., Yang et al. 2007; Zhao et al. 2012). High positive zircon ε_{Hf} (t) values are indicative of depleted mantle-derived magmas (e.g. Ma et al. 2013). Our samples had no mafic micro granular enclaves or specific textures, which implies magma mixing and mingling processes in their generation. The variable and usually positive zircon ε_{Hf} (t) values (from 4.6 to 13.5) with young single-stage Hf model ages (T_{DM1} = 0.30 to 0.65 Ga) demonstrate that heterogeneous depleted mantle components were involved in the melting source and the rocks were unlikely to be partial melts of a subducting oceanic slab. This is mirrored by the unique signature of the gabbroic rocks, which is inconsistent with those of experimental melts from infracrustal rocks such as metabasalts and eclogites with low Mg# (<43) values (Rapp and Watson 1995; Patiño Douce 1999).

The rocks were similar to the magma derived from partial melting of a ultramafic mantle, namely the depleted mantle, for which zircon ε_{Hf} (t) values are usually high and positive (Griffin et al. 2000; Ma et al. 2013). ε_{Hf} (t) values of an enriched lithospheric mantle and crustal materials are expected to be negative (Yang et al. 2006; Chen et al. 2008), which was not the case for the studied samples. The isotopic compositions of the gabbroic samples were less radiogenic than those of a depleted asthenospheric melt ($\varepsilon_{Nd}(t) = +5$; Basu et al. 1991). Their low Nb/La ratios are in complete accord with those of the lithospheric mantle (0.3–0.4) rather than OIB-like asthenospheric mantle melts (~>1; Bradshaw and Smith 1994; Smith et al. 1999). Additionally, the samples had uniform and relatively high Zr/Y (2–4) and Nb/Y (0.03–0.16) ratios, suggesting the melting of a depleted lithospheric mantle wedge. Moreover, high Sm/Yb (0.85–1.20) and La/Sm (1.60–4.07) values are consistent with the nature of a depleted lithospheric mantle composed of spinel-bearing lherzolite, which was confirmed by the trace-element modeling below. These features favor a source of depleted and young subcontinental lithospheric mantle rather than an enriched mantle or a juvenile mafic lower crust for the pluton. During the subduction events of the Paleo-Tethyan oceanic slab that began in the late Carboniferous period, deep slab dehydration caused a basaltic melt. Then, the basaltic melt triggered the partial melting of a depleted subcontinental lithospheric mantle wedge, possibly contributing to the generation of the gabbroic pluton. The relatively young single-stage Hf (T_{DM1} = 0.30 to 0.65 Ga) and Nd (T_{DM1} = 0.65 to 0.95 Ga) model ages point to a young subcontinental lithospheric mantle as a protolith and the lack of involvement of ancient crustal materials during partial melting. These suppositions are in accordance with the formation of the late Triassic to early Jurassic intrusive Zone. These intrusive rocks refer to subduction-related magmatism in the eastern Sakarya (Dokuz et al. 2006, 2017a; Karsli et al. 2014).

The primary magmas of the studied gabbroic samples may contain possible Al-phase types such as garnet and spinel during mantle melting at a great depth. Deeper sources can be inferred when the melting event occurred in the presence of garnet (i.e., melting of garnet-bearing mantle sources). Such melting resulted in fractionated MREE/HREE ratios, and hence negatively inclined the MREE to HREE patterns of the produced magmas on normalized REE plots. In contrast, spinel-bearing mantles do not result in fractionation of the MREE/HREE ratios of the resulting melts. The rocks produced by these ways are characterized by flatter MREE to HREE patterns. The MREE to HREE abundances of the gabbroic samples formed flat patterns on the chondrite-normalized REE diagram (Fig. 6a). The low $(Tb/Yb)_n$ values (0.90 to 1.28) of the samples reveal that they may have been produced in the absence of garnet in their mantle source (Ge et al. 2002). The melting histories of the gabbroic samples mirrored by the trace-element modeling of Gd/Yb versus La/Yb ratios of the rocks in Fig. 9. In the modeling diagram, primitive mantle (PM; Palme and O'Neil 2004), depleted- and enriched-depleted MORB mantles (D-DMM and E-DMM, respectively; Workmann and Hart 2005), and average E-MORB (Sun and McDonough 1989) are inserted to demonstrate the mantle array (gray field on Fig. 9). Importantly, the samples are plotted along the mantle array, indicating that MREE/HREE (Gd/Yb) fractionation did not occur during their genesis. The samples exhibit a positive trend with a slight variation in their Gd/Yb. This observation suggests that the primary magmas of the samples were derived from a shallower mantle source with the absence of garnet. The modeling results imply that low and variable portions (~5–15%) of partial melting of a depleted mantle material, which consists of spinel-bearing lherzolite, were apparent mechanisms for the generation of the samples. Fractional melting curves for both spinel- and garnet-bearing mantle mineralogy with PM trace-element composition are depicted in Fig. 9 to support these interpretations.

Metasomatism of depleted mantle source

The depleted isotopic signature of the Gokcedere gabbroic samples represent the mantle source prior to magma generation. The samples have depleted isotopic signature, but they show enrichment in their geochemical compositions due to mantle enrichment processes. Indeed, the samples exhibit slight enrichment of LILEs and LREEs with negative Nb and Ti anomalies, which are indicative of subduction-related magmas. These features are commonly attributed to a mantle source. However, how and when the enriched materials entered the mantle source of the Gokcedere gabbros remains debatable. Mantle materials in a mantle wedge are expected to have been previously

enriched in LILEs over HFSEs by the metasomatic activity of fluids derived from the subducted slab or sediments (e.g., Hawkesworth et al. 1997; Elburg et al. 2002; Cameron et al. 2003). An alternative metasomatism event is an interaction between the lithospheric mantle and the volatile-rich material of the asthenosphere (McKenzie 1989; Gibson et al. 1995). Such an enrichment is not the case for the geochemical character of the gabbroic pluton. Therefore, we propose that slab-derived fluids or sediment-related mantle enrichment played a major role in the generation of the pluton. Accordingly, the negative anomalies of Nb and Ti are typical of rocks formed in a subduction setting (Tatsumi and Kogiso 1997), which is consistent with the suggested model for the studied pluton. Hence, we assume that the mantle enrichment occurred during subduction of the Paleo-Tethyan oceanic lithosphere. In such a case, a large amount of fluid and/or sediment caused the metasomatization of the depleted mantle wedge prior to its partial melting. The samples exhibited high La/Ta (22–68) and low La/Ba (0.02–0.0.06) ratios, similar to those of a subcontinental lithosperic mantle modified by subduction processes (e.g., Zhou et al. 2005; Wang et al. 2013). The narrow range of the Th/Yb (0.27–1.42) and low Th/Ce (0.05–0.33) ratios of the samples reveal that subducted sediment materials may have had little or no joining in the mantle source. Elevation of the values of the samples is expected if a sedimentary addition formed, as suggested by Taylor et al. (1981) and Woodhead et al. (2001). Relatively low Sm/Th (0.78–4.11) and high Th/Y (0.03–0.14) ratios and variable Th/Zr (0.01–0.40), Ba/Th (522–194), Ba/La (15–47), and Ba/Nb (54–226) ratios of the samples are indicative of subducted slab-derived fluids in the source. This is further supported by the generally positive zircon $\varepsilon_{Hf}(t)$ values of the samples. Beccaluva et al. (2004) suggested that an important feature of subduction-related mantle metasomatism is the formation of the hydrous mineral phase phlogopite or amphibole (or both). The element compatibility of phlogopite and amphibole can indicate which hydrous phase was formed in the lithosperic mantle source during melting (Furman and Graham 1999; Yang et al. 2004). The most primitive sample of the pluton, GD19, had low Ba/Rb (5.0) and Nb/Th (2.0) ratios whereas its Rb/Sr ratio (0.05) was relatively high. This suggests that the source should have contained phlogopite rather than amphibole. Furthermore, the chondrite-normalized LREE patterns of the samples were variable and the differences in the REE patterns (Fig. 6a) can be attributed potentially to source heterogeneity in the generation. Relative depletion in MREE is expected in the chondrite-normalized REE patterns of the samples if amphibole is stable in the source (Ge et al. 2002). This is not the case for the Gokcedere gabbroic samples (Fig. 6a). Therefore, this evidence indicates presence of phlogopite in the source mineralogy during their
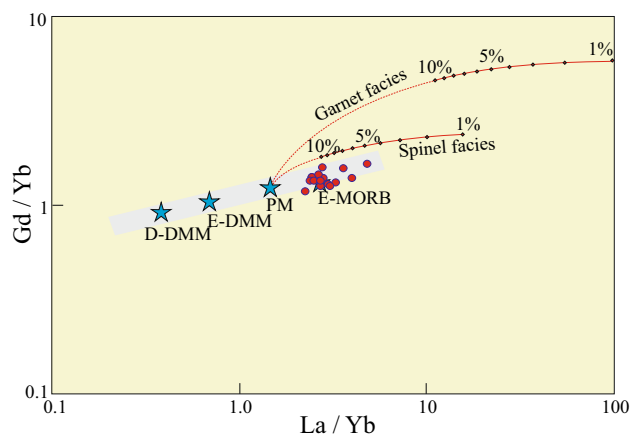
Fig. 9 The variation diagram of Gd/Yb versus La/Yb for the samples from the Gokcedere pluton. Also shown are primitive mantle (PM; Palme and O'Neil 2004), depleted- and enriched-depleted MORB mantles (D-DMM and E-DMM, respectively; Workmann and Hart 2005), and average E-MORB (Sun and McDonough 1989) to demonstrate the mantle array (*grey* field). Mineral and melt modes for spinel- and garnet facies mantle mineralogy are ol0.53(−0.06)+opx 0.27(0.28)+cpx0.17(0.67)+sp0.03(0.11) (Kinzler 1997) and ol0.60(0.03)+opx0.20(−0.16)+cpx0.10(0.88)+gt0.10(0.09) (Walter 1998), respectively. Melting curves with increments of 1–10% were calculated using non-modal fractional melting equation of Shaw (1970). The partition coefficients are from Adam and Green (2006)

generation. We can thus infer that the depleted source material was likely a phlogopite- and spinel-bearing lherzolite.

Implications for geodynamic processes and tectonic evolution

The Gokcedere gabbroic pluton formed in the eastern Sakarya Zone, where Carboniferous to late Triassic plutonic rocks are characterized by enriched mantle- and crustal-derived Sr–Nd isotopic compositions (Topuz et al. 2010; Dokuz 2011; Kaygusuz et al. 2012; Karsli et al. 2016). This indicates the occurrence of an enriched subcontinental lithospheric mantle and lower crustal material beneath the Sakarya Zone, northeast Turkey. However, the Gokcedere gabbroic samples have a relatively depleted Sr–Nd isotopic signature. Changes in the isotopic compositions of the resultant magmas represent changes in tectonic processes (Chu et al. 2011). High-precision LA-ICP-MS in situ zircon U–Pb techniques yielded weighted mean ages between 176.95 ± 0.49 Ma (MSWD = 1.08) and 178.41 ± 0.44 Ma (MSWD = 1.10) for the Gokcedere pluton, revealing its emplacement age. This age corresponds with the early Jurassic period in the region. Early Carboniferous to early Permian tectonothermal events are well known in the Sakarya Zone (Topuz et al. 2010; Dokuz 2011; Kaygusuz et al. 2012; Karsli

et al. 2016; Dokuz et al. 2017b). However, early Jurassic dynamic events are still debated due to limited data of the intrusive rocks. Therefore, understanding the early Mesozoic evolutional history of the region depends on the abundance of works on the early Jurassic magmatic rocks.

The calc-alkaline Gokcedere gabbroic pluton with a metaluminous and I-type signature exhibited enrichment in LREEs and LILEs and depletion in HREEs and HFSEs in the chondrite-normalized rare-earth element patterns and multi-element spidergrams. Such a geochemical fingerprint points geochemically to an enriched mantle wedge material and is also similar to that of an arc magmatic affinity described by (Sajona et al. (1996) and Stern and Kilian (1996). A few models have been suggested for magma generation from melting of a geochemically enriched mantle, namely (1) the magmatism resulting from the delamination of thickened continental crust due to arc- or continent–continent collision, (2) melting of an enriched mantle caused by large-scale extension (Thompson et al. 1989), (3) magmatism triggered by flat subduction of an oceanic slab (Li and Li 2007) or related slab window (Sun et al. 2007), and (4) magmatism in response to a back-arc setting related to subduction of the Paleo-Tethyan oceanic lithosphere. Subduction is believed to be responsible mechanism for the magma generation in the late Triassic-early Jurassic, as proposed by Dokuz et al. (2010) and Karsli et al. (2014). Indeed, collision-related magmatism for the Sakarya Zone is reported for the late Jurassic period (Dokuz et al. 2017a). Therefore, we can rule collisional magmatism out based on the available data. We can also omit the large-scale lithospheric extension as an alternative model due to the rarity of late Triassic to early Jurassic magmatism in the region. Similarly, wide temporal and spatial distribution of magmatism are expected if flat subduction and related slab window models generate gabbroic rock (Li and Li 2007; Sun et al. 2007). There is no evidence of flat subduction- and slab window-related magmatic activity in the area. Subsequently, we propose a back-arc setting related to subduction of the Paleo-Tethyan oceanic lithosphere because the sporadic nature of the intrusive rocks agrees well with the derivation from partial melting of an enriched lithospheric mantle beneath the Gondwana. This view is reinforced by trace-element variation diagrams (Pearce et al. 1984; Pearce 1996), which exhibit arc evolutionary trends. We attempt to use a plot of Rb versus Y + Nb, where the samples cluster into the volcanic arc granitoid (VAG) field (Fig. 10a) and the samples plot within the field of a pre-plate collision phase on the R1-R2 diagram (Batchelor and Bowden 1985), supplying tectonic discrimination for the granitoid plutons (Fig. 10b). This trend agrees with the clustering of the samples in the VAG field in Fig. 10a. In this model, the roll-back of the subducted slab is thought to

have provided upwelling of a hot asthenosphere, triggering partial melting of the mantle wedge (Fig. 11).

The early to middle Carboniferous period is referred to arc-continent collision and post-collision events, and many researchers have reached a consensus on this area (Topuz et al. 2010; Dokuz 2011; Kaygusuz et al. 2012; Dokuz et al. 2017b). However, subduction of the Paleo-Tethyan Oceanic lithosphere beneath the Gondwana has been suggested as starting start from the late Carboniferous to early Permian period (Karsli et al. 2016). We thus believe that the extensional events provided the emplacement of the pluton and may have no relationship with collision and post-collisional phases. Paleo-Tethyan oceanic subduction polarity in the region is still debated, and two models have been proposed. The southward subduction (Sengor and Yilmaz 1981; Sengor et al. 1984; Yilmaz et al. 1997; Dokuz et al. 2010) and northward subduction models (Robertson and Dixon 1984; Robinson et al. 1995; Ustaomer and Robertson 2010) have been proposed to explain the late Paleozoic to early Mesozoic tectonomagmatic events in the region. According to the northward subduction model, the Pontides are accepted as a continental margin bordering the Paleo-Tethyan Ocean on the north. In contrast, in the southward subduction model, the Pontides are referred to as the northern margin of Gondwana throughout the early Triassic to early Jurassic period. In this model, the Paleo-Tethyan oceanic lithosphere was southwardly subducted beneath the Gondwana until the middle Jurassic period, and the Cimmerian continent, including the eastern Sakarya Zone, was separated from the Gondwana due to the subduction event in the Triassic. These events resulted in the opening of an intra-continental back-arc basin. Closure of the Paleo-Tethyan Ocean led to an amalgamation of the eastern Sakarya Zone with the Laurasia during the middle Jurassic period (Sengor 1979; Sengor and Yilmaz 1981; Sengor et al. 1980, 1984; Yilmaz et al. 1997; Dokuz et al. 2010). Recent paleobiogeographical reconstructions, based on early Jurassic brachiopod fauna from the Sakarya Zone, indicate that the Cimmerian micro continent was far from the Gondwana and near the Eurasian margin of the Tethys (Vörös and Kandemir 2011). The position of the Cimmerian micro continent clearly supports the southward subduction model in the early Jurassic. This geodynamic model is also consistent with the generation of the early to middle Jurassic magmatism in the Yusufeli region in the eastern Sakarya Zone reported by Dokuz et al. (2010). What is more, the presence of Hardisi and Catalcesme Formations deposited in a marginal basin in the south of the area is also evidence for its southward subduction. In this case, the southward subduction of the Paleo-Tethyan oceanic slab is more consistent with the generation of the early Jurassic Gokcedere gabbroic pluton, based on its unique isotopical and geochemical signatures mentioned above. All of these results

are in accordance with the observations that the plutons were likely emplaced in an extensional setting during the late stage of the southward subduction of Paleo-Tethyan oceanic slab.

In summary, the tectonic affiliation and petrogenetic nature of the Gokcedere gabbroic pluton point to an origin in a late phase of a continental magmatic arc setting in response to southward subduction of the Paleo-Tethyan oceanic lithosphere beneath the Gondwana during early the Jurassic period. In the case of the southward subduction model, it was thought that the northern margin of the Paleo-Tethyan Ocean was passive. During its subduction, the dip angle of the subducted slab increased. Continental extension was induced by a roll-back of the slab as consequence of dipping and then the continental lithosphere was thinned by extension, as shown in Fig. 11. The back-arc lithospheric extension caused upwelling of the hot asthenosphere, which transferred heat energy into the mantle wedge, resulting in the partial melting of the depleted mantle wedge, which was metasomatized by fluids released by the subducted slab, formed beneath the continent. The parental basic melt may have been formed in this stage and the depleted mantle-derived basic magma subsequently evolved via crystal fractionation with no or minor crustal contamination during its ascent into the crust. Consequently, we conclude that the eastern part of the Sakarya Zone was favored by final phase of southward subduction of the Paleo-Tethyan oceanic lithosphere beneath the Gondwana throughout the early Jurassic period.

Conclusions

New in situ zircon U–Pb ages and Hf isotopes, whole-rock geochemical data, and Sr-Nd isotopes of a scarce volume gabbroic intrusion from the eastern Sakarya Zone (Bayburt area, NE-Turkey) provide constraints on the source, magma processes, and geodynamic events and reveal the following results in this work.

1. New in situ zircon U–Pb ages show igneous crystallization ages ranging from 176 to 178 Ma, corresponding with the early Jurassic period. We interpret this range as the likely emplacement age for the Gokcedere gabbroic pluton.

2. The early Jurassic gabbroic pluton has a metaluminous geochemical character and belongs to a slightly evolved I-type series. Its geochemical fingerprints and whole-rock Sr-Nd and in situ zircon Hf isotope compositions represent a depleted mantle source. Thus, a gabbroic pluton with a narrow range of rocks types may have been produced by partial melting of an isotopically depleted mantle wedge, which was subsequently
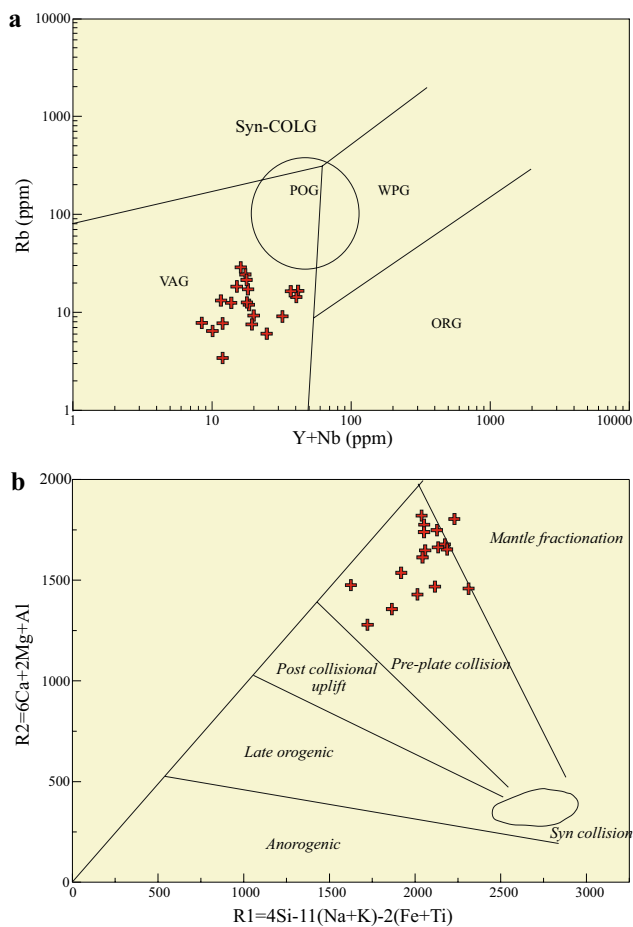
Fig. 10 Tectonic discrimination diagrams for the calc-alkaline Gokcedere pluton. **a** Rb versus Y + Nb (Pearce 1996; Pearce et al. 1984), *Syn-COLG* syn-collision granites; *WPG* within plate granites; *VAG* volcanic arc granites, *ORG* ocean ridge granites and **b** R1–R2 diagram of Batchelor and Bowden (1985) for the Gokcedere pluton. The samples mostly fall into the pre-plate collision field. R1 = 4Si−11(Na + K) − 2(Fe + Ti); R2 = 6Ca + 2Mg + Al
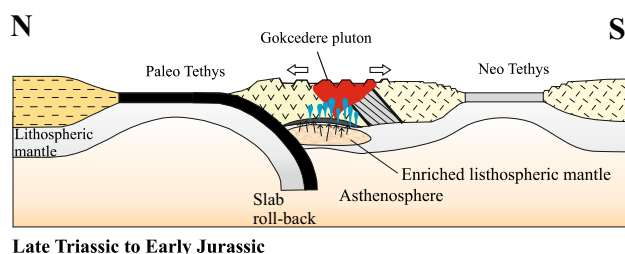

Fig. 11 Schematic diagram showing the Cimmerian geodynamic setting of the eastern Sakarya Zone where the Gokcedere gabbroic pluton was formed

role during its emplacement into the shallow depths of the crust. The modeling of trace-element abundances revealed that a low and variable degree of partial melting (~5–15%) of a depleted and young lithospheric mantle wedge consisting of phlogopite- and spinel-bearing lherzolite is responsible for the generation of the unique composition of the calc-alkaline gabbroic pluton. In such a dynamic system, upwelling of a hot asthenosphere triggered by roll-back of the slab in a subduction setting caused partial melting of the depleted mantle wedge.

3. The subduction of the Paleo-Tethyan oceanic lithosphere beneath the Gondwana continent commenced in the late Carboniferous to early Permian period. The roll-back events were a consequence of the late phase of subduction of the Paleo-Tethyan oceanic lithosphere formed during the late Triassic to early Jurassic periods. The integration of geological data with the new results of this study emphasizes that the final phase of southward subduction of the Paleo-Tethyan oceanic lithosphere during the Cimmerian Orogeny was responsible for the formation of the gabbroic rocks in a back-arc extensional setting as a consequence of slab roll-back.

References

Adam J, Green T (2006) Trace element partitioning between mica- and amphibole-bearing garnet lherzolite and hydrous basanitic melt: 1. Experimental results and the investigation of controls on partitioning behavior. Contrib Mineral Petrol 152:1–17

Altherr R, Topuz G, Siebel W, Sen C, Meyer H-P, Satir M (2008) Geochemical and Sr-Nd-Pb isotopic characteristics of Paleocene plagioleucitites from the Eastern Pontides (NE Turkey). Lithos 105:149–161

Aydin F (2014) Geocronology, geochemistry, and petrogenesis of the Maçka subvolcanic intrusions: implications for the late Cretaceous magmatic and geodynamic evolution of the eastern part of the Sakarya zone, northeastern Turkey. Int Geol Rev 56:1246–1275

Aydin F, Karsli O, Chen B (2008) Petrogenesis of the Neogene alkaline volcanics with implications for post collisional lithospheric thinning of the Eastern Pontides, NE Turkey. Lithos 104:249–266

Aydin F, Thompson R, Karsli O, Uchida H, Burt JB, Downs RT (2009) C2/c pyroxene phenocrysts from there potassic series in Neogene alkaline volcanics, Ne Turkey: their crystal chemistry

metasomatized by fluids released from the subducted slab. Fractional crystallization associated with minor or no crustal contamination appears to have played a

with petrogenetic significance as an indicator of P-T conditions. Contrib Min Petrol 158:131–147

Aydincakir E, Sen C (2013) Petrogenesis of the post collisional volcanic rocks from the Borçka (Artvin) area: Implications for the evolution of the Eocene magmatism in the Eastern Pontides. Lithos 172:98–117

Basu AR, Wang JW, Huang WK, Xie GH, Tatsumoto M (1991) Major element, REE, and Pb, Nd and Sr isotopic geochemistry of Cenozoic volcanic rocks of eastern China: implications for their origin from suboceanic-type mantle reservoirs. Earth Planet Sci Lett 150:149–169

Batchelor RA, Bowden P (1985) Petrogenetic interpretation of granitoid rock series using multicationic parameters. Chem Geol 48:43–55

Beccaluva L, Bianchini G, Bonadiman C, Siena F, Vaccaro C (2004) Coexisting anorogenic and subduction-related metasomatism in the mantle xenoliths from the Betic Cordillera (southern Spain). Lithos 75:67–87

Boynton WV (1984) Cosmochemistry of the rare earth elements: meteorite studies. In: Henderson P (Ed), Rare earth element geochemistry. Elsevier, Amsterdam, pp 63–114

Boztug D, Harlavan Y (2008) K-Ar ages of granitoids unrevel the stages of Neo-tethyan convergence in the Eastern Pontides and central Anatolia, Turkey. Int J Earth Sci 97:585–599

Boztug D, Jonckheere R, Wagner GA, Yegingil Z (2004) Slow Senonian and fast Paleocene-Early Eocene uplift of the granitoids in the Central Eastern Pontides, Turkey: apatite fission-track results. Tectonophysics 382:213–228

Boztug D, Ercin AI, Kurucelik MK, Goc D, Komur I, Iskenderoglu A (2006) Geochemical characteristics of the composite Kackar batholith generated in a Neo-Tethyan convergence system, eastern Pontides, Turkey. J Asian Earth Sci 27:286–302

Bradshaw TK, Smith EI (1994) Polygenetic Quaternary volcanism at Crater Flat, Nevada. J Volcanol Geother Research 63:165–182

Cameron BI, Walker JA, Carr MJ, Patino LC, Matias O, Feigenson MD (2003) Flux versus decompression melting at stratovolcanos in southeastern Guatemala. J Volcanol Geother Res 119:21–50

Capkinoglu S (2003) First records of conodonts from the Permo-Carboniferous of Demirözü (Bayburt), Eastern Pontides, NE Turkey. Turkish J. Earth Sci 12:199–217

Castro A, Moreno-Ventas I, Dela Rosa JD (1991) H-type (hybrid) granitoids: a proposed revision of the granite-type classification and nomenculature. Earth Sci Rev 31:237–253

Chappell BW, White AJR (1992) I- and S-type granites in the Lachlan Fold Belt. Trans. Royal Soc Edinburg. Earth Sci 83:1–26

Chen B, Tian W, Jahn BM, Chen ZC (2008) Zircon SHRIMP U–Pb age and in-situ Hf isotopic analysis for the Mesozoic intrusion in South Taihang, North China craton: evidence for hybridization between mantle-derived magmas and crustal components. Lithos 102:118–137

Chu M-F, Chung S-L, O'Reilly SY, Pearson NJ, Wu F-Y, Li X-H, Liu D, Ji J, Chu C-H, Lee H-Y (2011) India's hidden inputs to Tibetan orogeny revealed by Hf isotopes of Transhimalayan zircons and host rocks. Earth Planet Sci Lett 307:479–486

Cinku MC, Ustaomer T, Hirt AM, Hisarli ZM, Heler F, Orbay N (2010) Southward migration of arc magmatism during latest Cretaceous associated with slab steepening, East Pontides, N Turkey: New paleomagnetic data from the Amasya region. Phys Earth Planet Inter 182:18–29

Defant MJ, Drummond MS (1990) Derivation of some modern arc magmas by melting of young subducted lithosphere. Nature 347:662–665

Dokuz A (2011) A slab detachment and delamination model for the generation of Carboniferous high-potassium I-type magmatism in the Eastern Pontides, NE Turkey: Kose composite pluton. Gond Res 19:926–944

Dokuz A, Tanyolu E (2006) Geochemical constrains on the provenance, mineral sorting and subaerial weathering of Lower Jurassic and Upper Cretaceous clastic rocks from the eastern Pontides, Yusufeli (Artvin), NE Turkey. Turk J Earth Sci 15:181–209

Dokuz A, Tanyolu E, Genc S (2006) A mantle- and a lower crust-derived bimodal suite in the Yusufeli (Artvin) area, NE Turkey: trace element and REE evidence for subduction-related rift origin of Early Jurassic Demirkent intrusive complex. Int J Earth Sci 95:370–394

Dokuz A, Karsli O, Chen B, Uysal I (2010) Sources and petrogenesis of Jurassic granitoids in the Yusufeli area, Northeastern Turkey: implication for pre- and post-collisional lithospheric thinning of the Eastern Pontides. Tectonophysics 480:259–279

Dokuz A, Uysal I, Kaliwoda M, Karsli O, Ottley CJ, Kandemir R (2011) Early abyssal- and late SSZ-type vestiges of the Rheic oceanic mantle in the Variscan basement of the Sakarya Zone, NE Turkey: implications for the sense of subduction and opening of the Paleotethys. Lithos 127:176–191

Dokuz A, Uysal I, Siebel W, Turan M, Duncan R, Akcay M (2013) Post-collisional adakitic volcanism in the eastern part of the Sakarya Zone, Turkey: evidence for slab and crustal melting. Contrib Min Petrol 166:1443–1468

Dokuz A, Aydincakir E, Kandemir R, Karsli O, Siebel W, Derman AS, Turan M (2017a) Late Jurassic magmatism and stratigraphy in the eastern Sakarya zone, Turkey. Evidence for the slab breakoff of Paleotethyan oceanic crust. J Geol 125:1–31

Dokuz A, Külekçi E, Aydınçakır E, Kandemir R, Alçiçek MC, Pecha ME, Sünnetçi K (2017b) Cordierite-bearing strongly peraluminous Cebre Rhyolite from the eastern Sakarya zone, NE Turkey: Constraints on the Variscan Orogeny. Lithos 278–281:285–302

Elburg MA, Bergen MV, Hoogewerff J, Foden J, Vroon P, Zulkarnain I, Nasution A (2002) Geochemical trends across an arc-continent collision zone: magma sources and slab-wedge transfer processes below the Pantar Strait volcanoes, Indonesia. Geochim Cosmos Acta 66:2771–2789

Eyuboglu Y, Santosh M, Bektas O, Chung S-L (2011) Late Triassic subduction related ultramafic-mafic magmatism in the Amasya region (eastern Pontides, N Turkey): implications for the ophiolite conundrum in Eastern Mediterranean. J Asian Earth Sci 42:234–257

Frey FA, Green EH, Roy SD (1978) Integrated model of basalt petrogenesis: a study of quartz toleiities to olivine melilites from southeastern Australia, utilizing geochemical experimental data. J Petrol 19:463–513

Furman T, Graham D (1999) Erosion of lithospheric mantle beneath the East African Rift system: geochemical evidence from the Kivu volcanic province. Lithos 48:237–262

Ge XY, Li XH, Chen ZG, Li W (2002) Geochemistry and petrogenesis of Jurassic high Sr/low Y granitoids in the eastern China: constraints on crustal thickness. Chin Sci Bull 47: 962–968

Gibson SA, Thompson RN, Leonardos OH, Dickin AP, Mithchell JG (1995) The late Cretaceous impact of the Trindade mantle plume: evidence from large-volume, mafic, potassic magmatism in SE Brazil. J Petrol 36:189–229

Goncuoglu MC, Goncuoglu Y, Kozur HW, Kozlu H (2004) Paleozoic stratigraphy of Geyik Dagi unit in the Eastern Taurides (Turkey): new age data and implications for Gondwanan evolution. Geol Carpath 55:433–447

Gorur N (1997) Cretaceous syn-to post-rift sedimentation on the Southern Continental Margin of the Western Black Sea Basin. In: Robinson AG (ed), pp 227–240

Griffin WL, Pearson NJ, Belousova E, Jackson SE, van Achterbergh E, O'Reilly SY, Shee SR (2000) The Hf isotope composition of cratonic mantle: LAM-MC-ICPMS analysis of zircon megacrysts in kimberlites. Geochim Cosmos Acta 64:133–147

Griffin WL, Wang X, Jackson SE, Pearson NJ, O'Reilly SY, Xu XS, Zhou XM (2002) Zircon chemistry and magma mixing, SE China: in situ analysis of Hf isotopes, Tonglu and Pingtan igneous complexes. Lithos 61:237–269

Hawkesworth CJ, Turner SP, McDermott F, Peate DW, van Calsteren P (1997) U-Th isotopes in arc magmas: implications for element transfer from the subducted crust. Sciences 276:551–555

He ZY, Xu XS, Niu Y (2010) Petrogenesis and tectonic significance of a Mesozoic granite-syenite-gabbro association from inland South China. Lithos 119:621–641

Hisarli ZM (2011) Paleomagnetic constraints on the late Cretaceous and early Cenozoic tectonic history of the Eastern Pontides. J Geodynamics 52:114–128

Hoskin PWO, Schaltegger U (2003) The compositions of zircon and igneous and metamorphic petrogenesis. In: Hanchar JM, Hoskin PWO (Eds), Zircon Reviews in Mineralogy and Geochemistry 53. Mineral Soc America, Washington D.C, pp 27–62

Hou KJ, Li YH, Tian YY (2009) In situ U–Pb zircon dating using laser ablation-multi ion counting-ICP-MS. Min Depos 28:481–492

Kandemir R (2004) 'Gumushane yakin yorelerindeki Erken-Orta Jura yasli Şenköy Formasyonu'nun cokel ozellikleri ve birikim kosullari' KTU Fen Bilimleri Enstitusu, PhD Thesis (in Turkish with English abstract)

Kandemir R, Lerosey-Aubril R (2011) First report a trilobite in the Carboniferous of Eastern Pontides, NE Turkey. Turk J Earth Sci 20:179–183

Kandemir R, Yilmaz C (2009) Lithostratigraphy, facies, and deposition environment of the lower Jurassic Ammonitico Rosso type sediments (ARTS) in the Gümüşhane area, NE Turkey: implications for the opening of the northern branch of the Neo-Tethys Ocean. J Asian Earth Sci 34:586–598

Karsli O, Chen B, Aydin F, Sen C (2007) Geochemical and Sr-Nd-Pb isotopic compositions of the Eocene Dölek and Sariçiçek Plutons, Eastern Turkey: Implications for magma interaction in the genesis of high-K calc-alkaline granitoids in a post-collision extensional setting. Lithos 98:67–96

Karsli O, Dokuz A, Uysal I, Aydin F, Bin C, Kandemir R, Wijbrans RJ (2010a) Relative contributions of crust and mantle to generation of Campanian high-K calc-alkaline I-type granitoids in a subduction setting, with special reference to the Harşit pluton, Eastern Turkey. Contrib Min Petrol 160:467–487

Karsli O, Dokuz A, Uysal I, Aydin F, Kandemir R, Wijbrans RJ (2010b) Generation of the Early Cenozoic adakitic volcanism by partial melting of mafic lower crust, Eastern Turkey: implications for crustal thickening to delamination. Lithos 114:109–120

Karsli O, Uysal I, Ketenci M, Dokuz A, Aydin F, Kandemir R, Wijbrans J (2011) Adakite-like granitoid porphyries in Eastern Pontides, NE Turkey: potential parental melts and geodynamic implications. Lithos 127:354–372

Karsli O, Caran S, Dokuz A, Coban H, Bin C, Kandemir R (2012a) A-type granitoids from the Eastern Pontides, NE Turkey: records for generation of hybrid A-type rocks in a subduction-related environment. Tectonophysics 530–531:208–224

Karsli O, Dokuz A, Uysal I, Ketenci M, Chen B, Kandemir R (2012b) Deciphering the shoshonitic monzonites with I-type characteristic, the Sisdaği pluton, NE Turkey: Magmatic response to continental lithospheric thinning. J Asian Earth Sci 51:45–62

Karsli O, Dokuz A, Kaliwoda M, Uysal I, Aydin F, Kandemir R, Fehr KT, Wijbrans RJ (2014) Geochemical fingerprints of late Triassic calc-alkaline lamprophyres from the Eastern Pontides, NE Turkey: a key to understanding lamprophyre formation in a subduction-related environment. Lithos 196–197:181–197

Karsli O, Dokuz A, Kandemir R (2016) Subduction-related late Carboniferous to early Permian magmatism in the eastern Pontides, the Camlik and Casurluk plutons: Insights from geochemistry, whole-rock Sr-Nd and in situ zircon Lu-Hf isotopes, and U–Pb geochronology. Lithos 266–267:98–114

Kaygusuz A, Siebel W, Sen C, Satir M (2008) Petrochemistry and petrology of I-type granitoids in an arc setting: the composite Torul pluton, Eastern Pontides, NE Turkey. Int J Earth Sci 97:739–764

Kaygusuz A, Arslan M, Siebel W, Sipahi F, Ilbeyli N (2012) Geocronological evidence and tectonic significance of Carboniferous magmatism in the southwest Trabzon area, eastern Pontides, Turkey. Int Geol Rev 54: 1776–1800

Kemp AIS, Whitehouse MJ, Hawkesworth CJ, Alarcon MK (2005) A zircon U–Pb study of metaluminous (I-type) granites of the Lachlan Fold Belt, southeastern Australia: implications for the high/low temperature classification and magma differentiation processes. Contrib Mineral Petrol 150:230–249

Kinzler RJ (1997) Melting of mantle peridotite at pressures approaching the spinel to garnet transition: Application to midocean ridge basalt petrogenesis. J Geop Res 102:853–874

Kocyigit A, Altiner D (2002) Tectonostratigraphic evolution of the North Anatolian Paleorift (NAPR): Hettangian-Aptian passive continental margin of the Northern Neo-Tethys, Turkey. Turk J Earth Sci 11:169–191

Li ZX, Li XH (2007) Formation of the 1300-km-wide intracontinental orogeny and postorogenic magmatic province in Mesozoic South China. A flat-slab subduction model. Geology 35:179–182

Liu YS, Hu ZC, Gao S et al (2008) In situ analysis of major and trace elements of anhydrous minerals by LA-ICP-MS without applying an internal standard. Chem Geol 257:34–43

Ma X, Chen B, Chen JF, Niu XL (2013) Zircon SHRIMP U–Pb age, geochemical, Sr-Nd isotopic, and in-situ Hf isotopic data of the late Carboniferous-early Permian plutons in the northern margin of the North China Craton. China. Earth Sci 56:126–144

Mackintosh PW, Robertson AHF (2009) Structural and sedimentary evidence from the northern margin of the Tauride platform in south central Turkey used to test alternative models of Tethys during Early Mesozoic time. Tectonophysics 471:203–215

Mahoney JJ, Frei R, Tejada MLG, Mo XX, Leat PT, Nagler TP (1998) Tracing the Indian Ocean mantle domain through time: isotopic results from old west Indian, east Tethyan and South Pacific seafloor. J Petrol 39:1285–1306

Maniar PD, Piccoli PM (1989) Tectonic discrimination of granitoids. Bull Am Geol Soc 101:635–643

McKenzie DP (1989) Some remarks on the movement of small melt fractions in the mantle. Earth Planet Sci Lett 95:53–72

Middlemost EAK (1994) Naming materials in the magma/igneous rock system. Earth Sci Rev 37:215–224

Miller CF, McDowell SM, Mapes RW (2003) Hot and cold granites? Implications of zircon saturation temperatures and preservation of inheritance. Geology 31:529–532

Nasdala L, Norberg N, Schaltegger U et al (2008) Zircon M257: a homogeneous natural reference material for the ion microprobe U–Pb analysis of zircon. Geostand Geoanalytical Res 32:247–265

Okay AI, Goncuoglu MC (2004) The Karakaya complex: a review of data and concepts. Turk J Earth Sci 13(2):77–95

Okay AI, Leven EJ (1996) Stratigraphy and paleontology of the upper Paleozoic sequences in the Pulur (Bayburt) region, Eastern Pontides. Turk J Earth Sci 5:145–155

Okay AI, Sahinturk O (1997) Geology of the Eastern Pontides. In: Robinson AG (Ed.) Regional and Petroleum Geology

of the Black Sea and Surrounding Region. AAPG Memoir 68:292–311

Okay AI, Tuysuz O (1999) Tthyan sutures of northern Turkey. In: "The Mediterranean Basins: Tertiary extension within the Alpine oregon" (eds. Durand B, Jolivet L, Horvath F, Seranne M), Geol Soc, London, Spec Public, vol 156, pp 475–515

Okay AI, Sengor AMC, Gorur N (1994) Kinematic history of the opening of the Black Sea and its effect on the surrounding regions. Geology 22:267–270

Okay AI, Monod O, Monie P (2002) Triassic bluechists and eclogites from northwest Turkey: vestiges of the Paleo-Tethyan subduction. Lithos 64(3–4):155–178

Okay AI, Satir M, Siebel W (2006) Pre-Alpide Paleozoic and Mesozoic orogenic events in the Eastern Mediterranean region. Geol Soc Lond Memoir 32:389–405

Palme H, O'Neill HSC (2004) Cosmochemical estimates of mantle composition. In: Holland HD, Turekian KK (eds) Treatise on Geochemistry, 2. Elsevier, Amsterdam, pp 1–38

Patiño Douce AE (1999) What do experiments tell us about the relative contributions of crust and mantle to the origin of granitic magmas? In: Castro A, Fernandez C, Vigneresse JL (Eds), Understanding granites: integrating new and classical techniques. Geol Soc London, vol 168, pp 55–75

Pearce JA (1996) Sources and settings of granitic rocks. Episodes 19:120–125

Pearce JA, Harris NBW, Tindle AG (1984) Trace element discrimination diagrams for the tectonic interpretation of granitic rocks. J Petrol 25:956–983

Peccerillo A, Taylor SR (1976) Geochemistry of Eocene calc-alkaline volcanic rocks from Kastamonu area, northern Turkey. Contrib Min Petrol 58:63–81

Pouchou JL, Pichoir F (1985) "PAP" (ø.ρ.Z) correction procedyre for improved quantitative microanalysis. In: Armstrong JT (Ed) Microbeam analysis. San Francisco Press, pp 104–106

Qiao G (1988) Normalization of isotopic dilution analyses-a new program for isotope mass spectrometric analysis. Sci Sin 31:1263–1268

Rapp RP, Watson EB (1995) Dehydration melting of metabasalt at 8–32 kbar: implications for continental growth and crust-mantle recycling. J Petrol 36:891–931

Robertson AHF, Dixon JE (1984) Introduction: aspects of the geological evolution of the eastern Mediterranean. In: Dixon JE, Robertson AHF (Eds) The geological evolution of the Eastern Mediterranean. Geol Soc London Spec Publicm, vol 17, pp 1–74

Robertson AHF, Ustaomer T, Pickett EA, Collins AS, Dixon JE (2004) testing models of late Paleozoic-early Mesozoic orogeny in Western Turkey: support for an evolving open-Tethys model. J Geol Soc, London 161:501–511

Robinson AG, Banks CJ, Rutherford MM, Hirst JPP (1995) Stratigraphic and structural development of the Eastern Pontides, Turkey. J Geol Soci Lond 152:861–872

Rolland Y, Perincek D, Kaymakci N, Sosson M, Barrier E, Avagyan A (2012) Evidence for ~80–75 Ma subduction jump during Anatolia-Tauride-Armenian block accretion and ~48 Ma Arabia-Eurasia collision in Lesser Caucasus-East Anatolia. J Geodyn 56–57:76–85

Sajona FG, Maury RC, Bellon H, Cotton J, Defant M (1996) High field strength element enrichment of Pliocene-Pleistocene Isand Arc Basalts, Zamboanga Peninsula, Western Mindanao (Philippines). J Petrol 37:693–726

Sen C (2007) Jurassic volcanism in the Eastern Pontides: is it rift related or subduction related? Turk J Earth Sci 16:523–539

Sengor AMC (1979) Mid-Mesozoic closure of Permo-Triassic Tethys and its implications. Nature 279:590–593

Sengor AMC, Yilmaz Y (1981) Tethyan evolution of Turkey: a plate tectonic approach. Tectonophysics 75:181–241

Sengor AMC, Yilmaz Y, Ketin I (1980) Remnants of Pre-Late Jurassic Ocean in northern Turkey: fragments of Permian-Triassic Paleo-Tethys. Geol Soc Am Bull 91:599–609

Sengor AMC, Yilmaz Y, Sungurlu O (1984) Tectonics of Mediterranean Cimmerides: nature and evolution of the western termination of Paleotethys. In: Dixon JE, Robertson AHF, (Eds). The Geological Evolution of the Eastern Mediterranean. Geol Soc London, Spec Public, vol 17, pp 77–112

Sengor AMC, Ozeren S, Genc T, Zor E (2003) East Anatolian high plateau as a mantle-supported, North-south shortened domal structure. Geophys Res Lett 30(24):8045. doi:10.1029/2003GL017858

Shaw DM (1970) Trace element fractionation during anatexis. Geochim Cosmochim Acta 34:237–243

Smith EI, Sánchez A, Walker JD, Wang K (1999) Geochemistry of mafic magmas in the Hurricane Volcanic field, Utah: implications for small- and large- scale chemical variability of the lithospheric mantle. J Geol 107:433–448

Söderlund U, Patchett JP, Vervoort JD, Isachsen CE (2004) The ^{176}Lu decay constant determined by Lu-Hf and U-Pb isotope systematics of Precambrian mafic intrusions. Earth Planet Sci Lett 219:311–324

Stern CR, Kilian R (1996) Role of the subducted slab, mantle wedge and continental crust in the generation of adakites from the Andean Austral Volcanic Zone. Contrib Min Petrol 123(3):263–281

Sun SS, McDonough WE (1989) Chemical and isotopic systematics of oceanic basalts: Implications for mantle composition and processes. In: Saunders AD, Norry MJ (Eds), Magmatism in the Ocean Basins. Special Publication. Geol Soc London, pp 313–345

Sun WD, Ding X, Hu YH, Li XH (2007) The golden transformation of the Cretaceous plate subduction in the west pacific. Earth Planet Sci Lett 262:533–542

Tatsumi Y, Kogiso T (1997) Trace element transport during dehydration processes in the subducted oceanic crust: 2. origin of chemical and physical characteristics in arc magmatism. Earth Planet Sci Lett 148:207–210

Taylor SR, McLennan, SM, Armstrong RL (1981) The composition and evolution of the continental crust: rare earth element evidence from sedimentary rocks and discussion. Philos Trans Roy Soc London Series A Math Phys Sci 301:381–399

Thompson RN, Leat P, Dickin AP, Morrison MA, Hendry GL, Gibson SA (1989) Strongly potassic mafic magmas from lithospheric mantle sources during continental extension and heating: evidence from Miocene minettes of northwest Colorado, U.S.A. Earth Planet Sci Lett 98:139–153

Topuz G, Altherr R, Kalt A, Satir M, Werner O, Schwarz WH (2004) Aluminous granulites from the Pulur complex, NE Turkey: a case of partial melting, efficient melt extraction and crystallization. Lithos 72:183–207

Topuz G, Altherr R, Schwarz WH, Siebel W, Satir M, Dokuz A (2005) Post-collisional plutonism with adakite-like signatures: the Eocene Saraycik granodiorite (Eastern Pontides, Turkey). Contrib Min Petrol 150:441–455

Topuz G, Altherr R, Schwarz WH, Dokuz A, Meyer HP (2007) Variscan amphibolite-facies rocks from the Kurtoğlu metamorphic complex. Gümüşhane area, Eastern Pontides, Turkey. Int J Earth Sci 96:861–873

Topuz G, Altherr R, Siebel W, Schwarz WH, Zack T, Hasözbek A, Mathias B, Satir M, Şen C (2010) Carboniferous high-potassium I-type granitoid magmatism in the Eastern Pontides: The Gümüşhane pluton (NE Turkey). Lithos 116:92–110

Topuz G, Gocmengil G, Rolland Y, Celik OF, Zack T, Schmitt AK (2013) Jurassic accretionary complex and ophiolite from

northeast Turkey: No evidence for the Cimmerian continental ribbon. Geology 41:255–258

Tribuzio R, Thirlwall MF, Vannucci R, Matthew F (2004) Origin of the gabbro-peridotite association from the Northern Apennine Ophiolites (Italy). J Petrol 45:1109–1124

Tuysuz O (1999) Geology of the Cretaceous sedimentary basins of the Western Pontides. Geol J 34:75–93

Ustaomer T, Robertson HFA (2010) Late Paleozoic-Early Cenozoic tectonic development of the Eastern Pontides (Artvin area), Turkey: stages of closure of Tethys along the southern margin of Eurasia. Spec Public, Geol Soc London 340:281–327

Vörös A, Kandemir R (2011) A new early Jurassic brachiopod fauna from the Eastern Pontides (Turkey). Neues Jb Geol PalÓ"ont Abh 260:343–363

Walter MJ (1998) Melting of garnet peridotite and the origin of komatiite and depleted lithosphere. J Petrol 39:29–60

Wang Y, Fu JY, Na FC, Liu YC, Zhang GY, Kang Z, Yang F (2013) Geochemical characteristics and zircon U–Pb age of the gabbrodiorite in Jalaid Banner of Inner Mongolia and their geological significance. Geol Bull China 32:1525–1535

Watson EB, Harrison TM (1983) Zircon saturation revisited: temperature and composition effects in a variety of crustal magma types. Earth Planet Sci Lett 64:295–304

Woodhead JD, Hergt JM, Davidson JP, Eggins SM (2001) Hafnium isotope evidence for conservative element mobility during subduction zone processes. Earth Planet Sci Lett 192:331–346

Workman RK, Hart SR (2005) Major and trace element composition of the depleted MORB mantle (DMM). Earth Planet Sci Lett 231:53–72

Wu FY, Yang YH, Xie LW, Yang JH, Xu P (2006) Hf isotopic composition of the standard zircons and baddeleyites used in U–Pb geochronology. Chem Geol 234:105–126

Wu FY, Li XH, Zheng YF, Gao S (2007) Lu-Hf isotopic systematics and their applications in petrology. Acta petrol Sin 23(2):185–220

Xu JF, Castillo PR, Chen FR, Niu HC, Yu XY, Zhen ZP (2003) Geochemistry of late Paleozoic mafic igneous rocks from the Kuerti area, Xinjiang, northwest China: implications for backarc mantle evolution. Chem Geol 193:137–154

Yang JH, Chung SI, Zhai MG, Zhou XH (2004) Geochemical and Sr-Nd-Pb isotopic compositions of mafic dykes from the Jiaodong peninsula, China: evidence for vein-plus-peridotite melting in the lithospheric mantle. Lithos 73:145–160

Yang JH, Wu FY, Chung SL, Wilde SA, Chu MF (2006) A hybrid origin for the Qianshan A-type granite, northeast China: geochemical and Sr-Nd-Hf isotopic evidence. Lithos 89:89–106

Yang JH, Wu FY, Wilde SA, Xie LW, Yang YH, Liu XM (2007) Tracing magma mixing in granite genesis: in situ U–Pb dating and Hf isotope analysis of zircons. Contrib Min Petrol 53:177–179

Yilmaz S, Boztug D (1996) Space and time relations of three plutonic phases in the Eastern Pontides, Turkey. Int Geol Rev 38:935–956

Yilmaz Y, Tuysuz O, Yigitbas E, Genc SC, Sengor AMC (1997) Geology and tectonic evolution of the Pontides. In: Robinson AG (ed) Regional and petroleum geology of the Black Sea and surrounding region. Am. Assoc Petrol Geo. Mem, vol 68, pp 183–226

Zhao KD, Jiang SY, Yang SY, Dai BZ, Lu JJ (2012) Mineral chemistry, trace elements and Sr-Nd-Hf isotope geochemistry and petrogenesis of Cailing and Furong granites and mafic enclaves from the Qitianling batholith in the SiHang zone, South China. Gond Res 22:310–324

Zhou CY, Wu FY, Ge WC, Sun DY, Abdel Rahman AA, Zhang JH, Cheng RY (2005) Age, geochemistry and petrogenesis of the cumulate gabbro in Tahe, northern Great Xing'an Range. Acta Petrol Sin 21:763–775